Nanoscale

ROYAL SOCIETY OF CHEMISTRY

REVIEW

View Article Online
View Journal | View Issue

Cite this: *Nanoscale*, 2024, **16**, 5487

Metal–organic framework-based S-scheme heterojunction photocatalysts

Ling Yuan,[b] Peiyang Du,[b] Luli Yin,[a] Jiamin Yao,[a] Jing Wang*[a] and Chao Liu *[b]

Photocatalysis is a promising technology to resolve energy and environmental issues, where the design of high-efficiency photocatalysts is the central task. As an emerging family of photocatalysts, semiconducting metal–organic frameworks (MOFs) with remarkable features have demonstrated great potential in various photocatalytic fields. Compared to MOF-based photocatalysts with a single component, construction of S-scheme heterojunctions can render MOFs with enhanced charge separation, redox capacity and solar energy utilization, and thus improved photocatalytic performance. Herein, an overview of the recent advances in the design of MOF-based S-scheme heterojunctions for photocatalytic applications is provided. The basic principle of S-scheme heterojunctions is introduced. Then, three types of MOF-based S-scheme heterojunctions with different compositions are systematically summarized including MOF/non-MOF, MOF-on-MOF and MOF-derived heterojunctions. Afterwards, the enhanced performances of MOF-based S-scheme heterojunctions in hydrogen production, CO_2 reduction, C–H functionalization, H_2O_2 production and wastewater treatment are highlighted. Lastly, the current challenges and future prospects regarding the design and applications of MOF-based S-scheme heterojunctions are discussed to inspire the further development of this emerging field.

Received 31st December 2023,
Accepted 5th February 2024

DOI: 10.1039/d3nr06677k

rsc.li/nanoscale

1. Introduction

The energy crisis and environmental pollution have become two worldwide challenges faced by human society. To resolve these problems, photocatalysis technology offers a promising strategy.[1,2] Using the powerful and inexhaustible solar energy as an energy input, photocatalysis can not only produce valuable chemicals, but also remediate environmental damage by degrading pollutants.[3,4] Currently, the greatest bottleneck of photocatalysis is the low photocatalytic efficiency caused by rapid electron–hole recombination and poor light harvesting ability.[5]

Over the past few decades, major efforts have been devoted to the exploration of high-efficiency photocatalysts. Plenty of semiconducting materials including metal oxides,[6,7] metal sulfides,[8,9] metal phosphides,[10,11] metal oxyhalides,[12,13] C_3N_4[14,15] covalent organic frameworks (COFs),[16,17] and metal–

[a]*School of Chemical and Environmental Engineering, Shanghai Institute of Technology, Shanghai 201418, P.R. China. E-mail: jingwang@sit.edu.cn*
[b]*School of Chemistry and Molecular Engineering, East China Normal University, Shanghai 200241, P.R. China. E-mail: cliu@chem.ecnu.edu.cn*

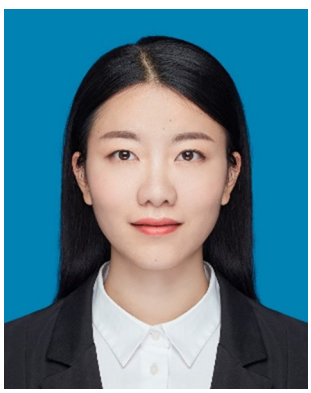

Ling Yuan

Ling Yuan is currently a Ph.D. student under the supervision of Prof. Chao Liu and Prof. Chengzhong Yu at East China Normal University. Her research field is MOF-based nanomaterials for applications in photocatalysis.

Jing Wang

Jing Wang received her Ph.D. degree (2018) from Nanjing University of Science and Technology. She worked as a postdoctoral fellow in Prof. Chengzhong Yu's group at East China Normal University (2018–2022). She is currently an associate professor at the Shanghai Institute of Technology. Her research focuses on the design of functional nanomaterials for environmental remediation and electrocatalysis.

organic frameworks (MOFs)[18,19] have been reported as photocatalysts for various photocatalytic reactions. Among them, MOFs, known as a type of porous crystalline material, have received specific attention.[20,21] Owing to their excellent physicochemical properties such as a large specific surface area, high porosity, dispersed metal sites and a ligand–metal charge transfer pathway,[4,22] semiconducting MOFs have demonstrated great potential in pollutant degradation,[23] water splitting,[24] organic transformation,[25] CO_2 reduction[26] and N_2 fixation.[27] Through precise regulation of the structures (*e.g.* pore space) and/or compositions (*e.g.* metal and/or ligand types) of MOFs, high activity and selectivity can be achieved in specific reactions.[18,19,28] Even so, for pristine MOFs with single compositions, the easy recombination of photocarriers restricts their photocatalytic performances.[29,30]

To improve their photocatalytic activity, several modification strategies including introducing defects,[28,31] doping heterometals/ligands,[32,33] loading co-catalysts and constructing heterojunctions have been developed.[34,35] Compared to other strategies, heterojunction construction by integrating two semiconductors with different band structures exhibits unique advantages in promoting charge separation.[36–38] To date, numerous organic or inorganic semiconductors such as COFs,[37] hydrogen-bonded organic frameworks (HOFs),[38] metal sulfides,[39] metal oxides[40] and metal hydroxides[41] have been adopted for coupling with MOFs, resulting in MOF-based heterojunctions with different working mechanisms. Among them, the step-scheme (S-scheme) charge transfer mechanism stands out because it can significantly facilitate photogenerated electron–hole separation and maximally preserve the redox ability of semiconducting units. Inspiringly, the design and application of MOF-based S-scheme heterojunction photocatalysts has thus become a rapidly expanding field. Synthetic strategies including hydro/solvothermal treatment, the impregnation method and high-temperature pyrolysis have been developed for the fabrication of MOF-based S-scheme heterojunctions with controllable components.[40,42,43] Their applications have also been investigated from efficient hydrogen evolution, CO_2 reduction, organic synthesis, H_2O_2 production to pollutant degradation with enhanced activity compared to single MOFs.[42,44–46] For S-scheme heterojunctions, several excellent reviews have been contributed,[47–49] while a dedicated review of emerging MOF-based S-scheme heterojunctions is still lacking but highly desired. In this context, a timely summary on the recent advances of MOF-based S-scheme heterojunctions with regard to their synthesis, structures and applications is provided in this review (Scheme 1).

Firstly, a brief introduction of different types of heterojunctions is presented with a focus on their working mechanisms. Secondly, the obtained MOF-based S-scheme heterojunctions with different compositions are systematically outlined. Thirdly, the enhanced performances of the heterojunctions in various photocatalytic reactions are highlighted. Finally, the current challenges and future perspectives are discussed for promoting the further development of this fascinating field.

2. Different types of heterojunctions and their charge transfer mechanisms

Construction of heterojunction photocatalysts by conjugating two dissimilar semiconductors (semiconductors 1 and 2, denoted as S1 and S2) has been widely recognized as an important strategy to improve their photocatalytic activity by facilitating the separation and utilization of photogenerated electron–hole pairs.[5] The currently existing heterojunctions can be mainly divided into six types: type I with a straddling gap, type II with a staggered gap, type III with a broken gap, traditional Z-scheme, all-solid-state Z-scheme and S-scheme heterojunctions.[50] Their energy level structures are schematically pre-

Chao Liu

Chao Liu received his bachelor's (2012) and Ph.D. degrees (2018) from Nanjing University of Science and Technology. He worked as a postdoctoral fellow in Prof. Chengzhong Yu's group at East China Normal University (2018–2021). He is currently a professor at East China Normal University. His research focuses on the design and synthesis of nanostructured MOF materials for catalysis.

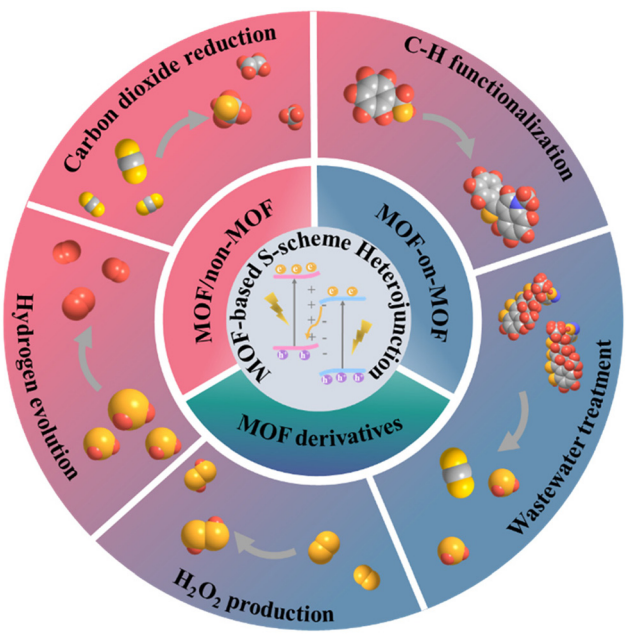

Scheme 1 An overview of the structures and applications of MOF-based S-scheme heterojunction photocatalysts.

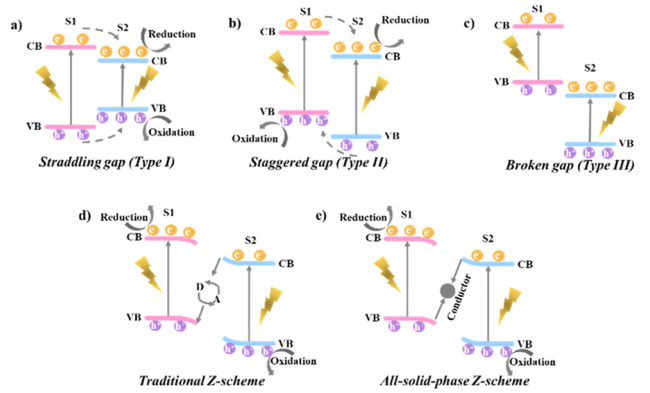

Fig. 1 Band structures and charge transfer directions in (a) straddling gap (type I), (b) staggered gap (type II), (c) broken gap (type III), (d) traditional Z-scheme, and (e) all-solid-state Z-scheme heterojunctions.

sented. For type-I heterojunctions (Fig. 1a), the conduction band (CB) and the valence band (VB) of semiconductor S2 straddle between the VB and the CB of semiconductor S1. The photogenerated electrons and holes are both accumulated on S2 with a small band gap, resulting in high recombination probability and weak redox ability.[51] For type-II heterojunctions (Fig. 1b), both the CB and VB positions of S1 are more negative than S2, forming a staggered alignment. As a result, the photogenerated electrons migrate from S1 to S2 with an adverse transfer direction of photogenerated holes, enabling a spatial separation of photogenerated electron–hole pairs. Nevertheless, there also exist several disadvantages that prevent the wide application of type-II heterojunctions. Because the CB level of S2 is more positive than that of S1 and the VB level of S1 is more negative than that of S2, the redox capability of both electrons and holes is reduced. In addition, the electrostatic repulsion from electrons in S2 and holes in S1 dramatically hinders the continuous electron/hole migration.[52] The band structure of type-III heterojunctions is similar to that of type-II heterojunctions except that the VB of S1 is higher than the CB of S2 without overlap between two semiconductors. In this case, the electron and hole transfer between S1 and S1 cannot take place (Fig. 1c).[53]

To address the problems faced by the above three types of heterojunctions, researchers developed a type of traditional Z-scheme heterojunction with ionic acceptor/donor (A/D) couples (*e.g.* Fe^{3+}/Fe^{2+}, I_3^-/I^-) inspired by the natural photosynthesis in plants (Fig. 1d).[54–56] During photocatalytic reactions, the photogenerated electrons on the CB of S2 transfer to the VB of S1 *via* the redox reactions between A/D pairs.[57] Typically, the electrons on the CB of S2 reduce A into D, and the D is subsequently oxidized into A by the holes on the VB of S1. On this basis, the electrons and holes are respectively accumulated on the CB of S1 and the VB of S2, giving higher reduction and oxidation potentials and spatial charge separation.[54,58] However, the application of such a system is limited in the solution phase and pH-sensitive redox ion pairs are inevitably needed with the undesired light shielding effect.[47] To broaden the application scope of the Z-scheme mechanism, all-solid-state Z-scheme heterojunctions are proposed, where the A/D pairs are replaced by a conductor as the electron mediator (Fig. 1e).[59] The integration of a conductor at the interface of S1 and S2 forms an ohmic contact with low electron transport resistance. The photogenerated electrons on the CB of S2 can directly migrate to the VB of S1 for consuming the holes, accomplishing the Z-scheme charge transfer pathway in an all-solid state with extended applications in solution, gas and solid media.[54,60,61] Even though promising, the electron mediates are generally noble metals with high cost, restricting the practical applications of these photocatalytic materials.[54]

In this context, an innovative heterojunction concept, named step-scheme (S-scheme) heterojunctions (the sixth type), was proposed by Yu's group in 2019 and 2020.[3,47,48] In an S-scheme heterojunction photocatalyst, a reduction photocatalyst (RP) and an oxidation photocatalyst (OP) with a staggered band structure are directly combined. The RP exhibits higher CB, VB and Fermi levels than the OP.[47] The charge transfer route within an S-scheme heterojunction is presented in Fig. 2. When in contact, the free electrons in RP diffuse spontaneously into OP due to the different Fermi levels. Until alignment, a built-in electric field pointing from RP to OP is created with upward and downward band bending of RP and OP, respectively. Under light irradiation, the photogenerated carriers were excited from the VB to the CB in both RP and OP, generating photoelectrons and holes. Driven by the band bending and interface electric field, the electrons in the CB of OP will recombine with the holes in the VB of RP, leaving powerful electrons in the CB of RP and holes in the VB of OP for participating in the reduction and oxidation reactions, respectively. Reasonably, the S-scheme heterojunction can not only effectively promote the spatial carrier separation, but also maximize the photocatalytic redox capacity to greatly improve the photocatalytic activity.[48]

3. Methods for identifying the S-scheme charge transfer mechanism

To probe the proposed charge transfer pathway in S-scheme heterojunctions, advanced techniques including *in situ* irradiated X-ray photoelectron spectroscopy (ISIXPS), Kelvin probe

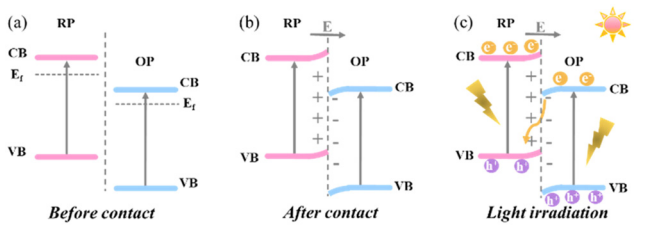

Fig. 2 Graphical illustration of the charge migration process of S-scheme heterojunctions. (a) before contact; (b) after contact; and (c) photogenerated charge carrier transfer under light irradiation.

force microscopy (KPFM), electron paramagnetic resonance (EPR) spectroscopy and density functional theory (DFT) calculations can provide direct evidence. The working principles of these methods will be discussed in the following sections with the combination of typical examples.

3.1 ISIXPS

XPS is an analytical technique that can sensitively detect the changes in the elemental binding energy and chemical environment, also referred to as the chemical shift.[62–64] The chemical shift caused by the variation in the valence state and electron density can be facilely determined by the binding energy shift in XPS spectra. Generally, the binding energy decreases by obtaining electrons, while increases by losing electrons.[47] On this basis, the electron transfer within the S-scheme heterojunctions is able to be measured by comparing the binding energies of RP and OP with and without light illumination. Once the contact is formed in the dark, the electron transfer from RP to OP will increase the binding energy of RP and decrease the binding energy of OP. Under irradiation, an opposite change will be observed by S-scheme charge transfer. Given that the S-scheme and type-II heterojunctions have completely different carrier migration pathways, ISIXPS characterization has been extensively adopted for differentiating these two types of heterojunctions.[65] For example, Xu *et al.* reported an $SnO_2/Cs_3Bi_2Br_9$ (SC4) S-scheme heterojunction *via* the electrostatic self-assembly of SnO_2 nanofibers and lead-free $Cs_3Bi_2Br_9$ quantum dots (QDs).[66] *In situ* XPS under light and dark conditions was performed to determine the charge transfer mechanism (Fig. 3). In the absence of light, the binding energies of Sn 3d and O 1s in the heterojunction negatively shifted (Fig. 3a and b), whereas the binding energies of Bi 4f and Br 3d positively shifted (Fig. 3c and d) compared with those of single SnO_2 and $Cs_3Bi_2Br_9$, suggesting the electron migration from $Cs_3Bi_2Br_9$ to SnO_2. In the presence of light, the binding energies of the corresponding elements oppositely shifted with a reversed electron transfer direction, in agreement with the S-scheme mechanism.

3.2 KPFM

As a derivative of atomic force microscopy (AFM), KPFM can not only scan the surface morphology, but also monitor the surface potential.[44,67] For an S-scheme heterojunction, the photogenerated electrons and holes are accumulated on RP and OP under light irradiation, reflected by the increased and decreased surface potentials of OP and RP in KPFM, respectively.[68] As a typical example using KPFM to verify the S-scheme mechanism, Qiao *et al.* prepared a TiO_2/FePS3 (TF) S-scheme heterojunction photocatalyst by coupling TiO_2 and 2D FePS3 (FPS) nanosheets.[69] The AFM and KPFM results showed that there existed a surface potential difference between TiO_2 and FPS before exposure to light, corresponding to the formation of a built-in electric field pointing from FPS to TiO_2. After illumination, the surface potential of FPS and TiO_2 became lower and higher, respectively, following the charge transfer mechanism of S-scheme heterojunctions (Fig. 4a–d).

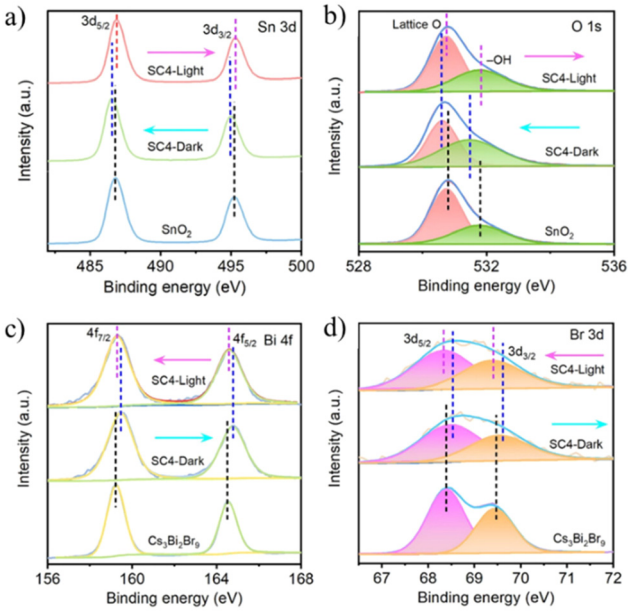

Fig. 3 High-resolution XPS spectra of (a) Sn 3d, (b) O 1s, (c) Bi 4f, and (d) Br 3d for SnO_2, $Cs_3Bi_2Br_9$, and SC4 obtained in the dark and under UV light irradiation, respectively. Reprinted with permission from ref. 66. Copyright 2023 American Chemical Society.

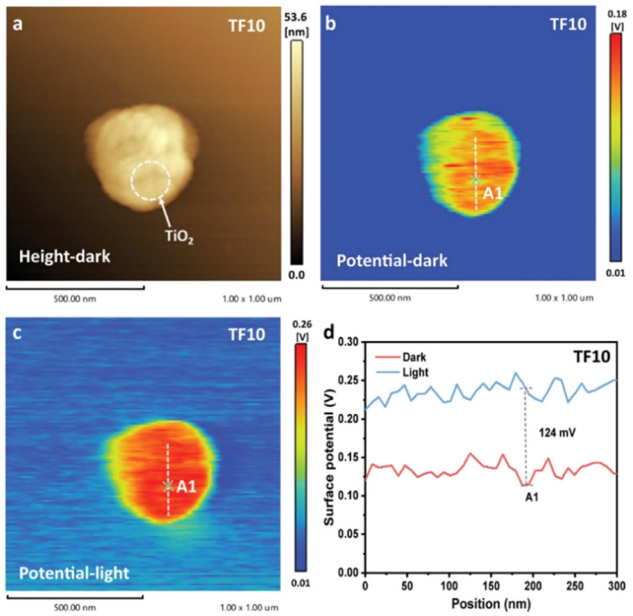

Fig. 4 (a) AFM and (b) KPFM images of TF in the absence of light. (c) KPFM image of TF under UV light illumination at 365 nm. (d) Corresponding surface potential profiles. Reprinted with permission from ref. 69. Copyright 2022 Wiley-VCH.

3.3 DFT calculations

Apart from experimental investigations, the electronic structures of heterojunctions can be simulated by DFT calculations, providing theoretical clues to help elucidate the charge

migration mechanism.[70–72] The crucial optical parameters including work function and density of states can be explored by DFT calculations. Moreover, the charge density difference (ΔP) between OP and RP can be directly utilized to disclose the interfacial electron transfer, where a positive and negative ΔP represents the electron accumulation and depletion, respectively. In other words, the interfacial electron transfer from RP to OP upon their contact in the dark gives a negative ΔP in RP and a positive ΔP in OP.[73,74] For instance, Zhang *et al.* investigated the enhanced catalytic performance over a $Cu_2V_2O_7$ (CVO)/α-Fe_2O_3 S-scheme heterojunction by DFT calculations.[75] The work functions of CVO (Fig. 5a) and Fe_2O_3 (Fig. 5b) were computed to be 5.09 and 6.87 eV, respectively. When the two components are in contact, Fe_2O_3 attracted the electrons from CVO until the Fermi energy level was equilibrated, creating a built-in electric field pointing from CVO with a negative ΔP to Fe_2O_3 with a positive ΔP (Fig. 5c). In addition, the charge density difference at the heterojunction interface between CVO and Fe_2O_3 was simulated to determine the charge transfer. The results in Fig. 5d show the electron transfer from CVO to Fe_2O_3. Thus, the CVO and Fe_2O_3 sides exhibit positive and negative charges, respectively, creating a built-in electric field at the interface (Fig. 5e).

3.4 EPR

Different from the above techniques that can provide direct evidence of charge transfer, EPR offers an indirect method for understanding the mechanism of S-scheme heterojunctions from the perspective of redox capability. Specifically, the radicals formed during the photocatalytic reaction, such as superoxide radicals ($^{\bullet}O_2^-$) requiring a strong reduction capability and hydroxyl radicals ($^{\bullet}OH$) requiring a strong oxidation capability, are detected by EPR. With the maximized redox power of S-scheme heterojunctions, higher EPR signals of $^{\bullet}OH$ and $^{\bullet}O_2^-$ radicals than OP and RP can be usually detected.[76–78] Following this principle, Wang *et al.* applied EPR to unveil the photocatalytic mechanism of the carbon quantum dot/Bi_2WO_6 (CQD/Bi_2WO_6) S-scheme heterojunction.[79] As displayed in Fig. 6a, b, d and e, only the EPR signal of $^{\bullet}O_2^-$ can be detected for CQDs as the RP under visible light, while for Bi_2WO_6 as the OP, the signal of $^{\bullet}O_2^-$ is invisible with identifiable $^{\bullet}OH$ signals. In contrast, through the combination of CQDs with Bi_2WO_6, the stronger signals of both $^{\bullet}O_2^-$ and $^{\bullet}OH$ are ascribed to the formation of an S-scheme heterojunction.

4. Synthesis and structures of MOF-based S-scheme photocatalysts

Given that MOF-based S-scheme photocatalysts can simultaneously integrate the merits of both semiconducting MOFs and S-scheme heterojunctions, significant efforts have been devoted to their synthesis. The resulting S-scheme heterojunctions can be approximately classified into the following types from the aspect of their components: MOF/non-MOF, MOF-on-MOF and MOF-derived S-scheme heterojunctions.

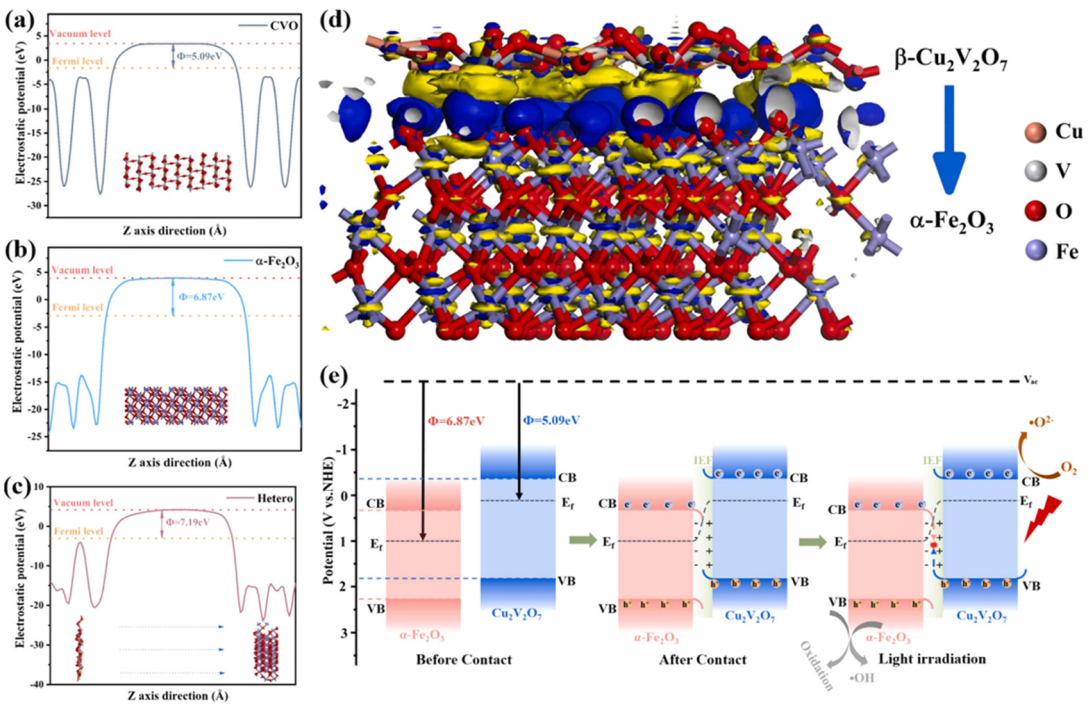

Fig. 5 Work functions of (a) CVO (010), (b) α-Fe_2O_3 (001), and (c) heterojunctions. (d) Charge density difference at the CVO (010)/α-Fe_2O_3 (001) interface, yellow indicates the loss of electrons and blue represents the gain of electrons. (e) Photocatalytic mechanism of S-scheme heterojunctions. Reprinted with permission from ref. 75. Copyright 2023 Elsevier.

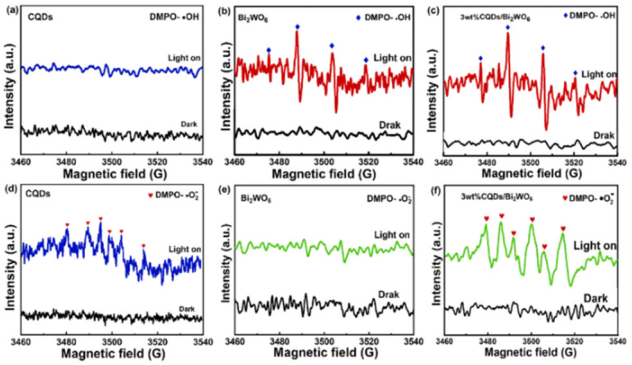

Fig. 6 EPR signals of CQDs, Bi_2WO_6, and 3 wt% CQDs/Bi_2WO_6 for DMPO-OH (a, b and c) and DMPO-O_2^- (d, e, and f). Reprinted with permission from ref. 79. Copyright 2023 Elsevier.

4.1 MOF/non-MOF heterojunctions

The abundant surface chemistry of MOFs endows them with great potential for hybridization with other functional materials toward S-scheme heterojunctions.[35] Various non-MOF semiconductors such as metal oxides,[40,45,80] metal sulfides,[81–84] metal phosphides,[85,86] and carbon-based composites[45,64,87] have been involved in synthetic routes including solvothermal treatment and the impregnation method. For example, Tang *et al.* reported a novel $CoFe_2O_4$/iron-based MOF (MIL-101, (MIL = Material Institute Lavoisier)) S-scheme heterojunction photocatalyst by a simple solvothermal method with $CoFe_2O_4$ nanoparticles distributed on the surface of MIL-101(Fe) octahedra (Fig. 7a).[40] In their synthesis, the pre-formed $CoFe_2O_4$ nanoparticles were *in situ* adhered onto the surface of MIL-101(Fe) octahedra by reacting with terephthalic acid (H_2BDC) and $FeCl_3$ $6H_2O$ in *N*,*N*-dimethylformamide (DMF) solution at 110 °C for 20 h. Using a similar procedure, an S-scheme heterojunction of zeolitic imidazolate framework-8 (ZIF-8)@Zn0.5Cd0.5S with sulfur vacancies (T-ZCSv) was also prepared (Fig. 7b).[84] Firstly, T-ZCSv was synthesized by the hydrothermal reaction of Zn$(CH_3CO_2)_2{\cdot}2H_2O$, Cd$(CH_3CO_2)_2{\cdot}2H_2O$ and CH_3CSNH_2 in 4 M NaOH at 180 °C for 24 h. The obtained T-ZCSv was then added to the reaction solution containing 1-methylimidazole (1-MeIM), 2-methylimidazole (2-MeIM) and $Zn(NO_3)_2{\cdot}6H_2O$ for aging in methanol solution at room temperature for 24 h. The resulting T-ZCSv exhibited a dodecahedral morphology with clear lattice fringes of Zn0.5Cd0.5S nanocrystals in different regions, consistent with the corresponding fast Fourier transform (FFT) patterns (Fig. 7c–e).

As well as metal oxides and metal sulfides, layered double hydroxides (LDHs) can also be merged with MOFs toward S-scheme heterojunctions.[41,42] As a typical example reported by Zhong and co-authors, a Ti-based NH_2-MIL-125 (NM) nanocake was synthesized *via* a one-pot solvothermal route as the substrate, followed by the growth of NiTi-LDH (NTL) nanosheets by a urea homogeneous precipitation method (Fig. 7f), forming MOF/LDH heterojunctions (NMNTL).[41] Different from the above studies, by adding non-MOF semiconductors during MOF growth or using MOFs as starting materials for the growth of non-MOF semiconductors, S-scheme heterojunctions with controllable compositions can also be obtained by partial pyrolysis of MOFs. For instance, through heat treatment of ZnCo-MOF at 300 °C under a PH_3 reducing atmosphere, Jin *et al.* constructed a ZnCo-MOF@CoP S-scheme heterojunction with the *in situ* generation of CoP nanocrystals on the surface of the preserved ZnCo-MOF (Fig. 7g).[86]

Carbon nitride (g-C_3N_4) is a fascinating metal-free conjugated polymer and one of the most widely studied semiconductors in various fields.[88–91] Recently, S-scheme heterojunctions prepared by the hybridization of g-C_3N_4 with MOFs have also been reported.[43,62] Vahid Safarifard's group reported the interfacial growth of four different cerium-based MOFs onto the surface of g-C_3N_4 *via* solvothermal treatment (Fig. 8a).[43] In the powder X-ray diffraction (XRD) pattern, the major diffraction peaks of both g-C_3N_4 and Ce-based MOFs (Ce-BDC, as a typical example) could be detected (Fig. 8b). Moreover, the N_2 adsorption–desorption isotherms of g-C_3N_4/Ce-BDC (Fig. 8c) exhibited type-III curves with an H3-type hysteresis loop, similar to those of Ce-BDC. Compared with C_3N_4, graphdiyne possesses a higher specific surface area and higher electrical conductivity, making it a promising candidate as a photocatalyst.[92–95] In this regard, Jin and coworkers decorated 2D graphdiyne (GDY) nanosheets onto 3D ZnCo-ZIF *via* impregnation treatment in water at 80 °C for 2 h, giving rise to a 2D/3D GDY/ZnCo-ZIF S-scheme heterojunction (Fig. 8d).[96] The TEM image presented the adhesion of GDY nanosheets on the surface of dodecahedral ZnCo-ZIF particles (Fig. 8e), effectively reducing the stacking of GDY nanosheets and promoting active site exposure.

The successful coupling of GDY and the ZnCo-ZIF was also verified by the typical diffraction peaks of both the ZnCo-ZIF and GDY (Fig. 8f).

As another emerging porous crystalline material, covalent organic frameworks (COFs) have attracted excessive research attention as photocatalysts because of their well-designed pore structure, constituting light elements (C, N, O), excellent stability, wide light absorption, *etc.*[16,97,98] The integration of two porous semiconducting materials, *i.e.*, MOFs and COFs, may perfectly inherit their merits with even additional properties generated.[99,100] Encouragingly, an olefin (C=C) linked-COF (TTCOF)/NH_2–UiO (UIO = University of Oslo)-66 (Zr) (NUZ) S-scheme heterojunction (TTCOF/NUZ) was prepared using TTCOF and NUZ as subunits *via* an *in situ* solvothermal strategy (Fig. 9a).[64] The XPS spectra (Fig. 9b) showed the existence of C, N, O and Zr elements. Fig. 9c displays the XRD patterns of TTCOF, NUZ, and TTCOF/NUZ samples. The XRD patterns of both TTCOF and NUZ well matched with the simulated one. For TTCOF/NUZ, the strong peaks mainly originated from NUZ due to its relatively high intensity. By enlarging the pattern, a weak reflection of the (100) plane corresponding to the mesoporous structure of TTCOF was found (Fig. 9c), suggesting the successful synthesis of TTCOF/NUZ hybrid materials.

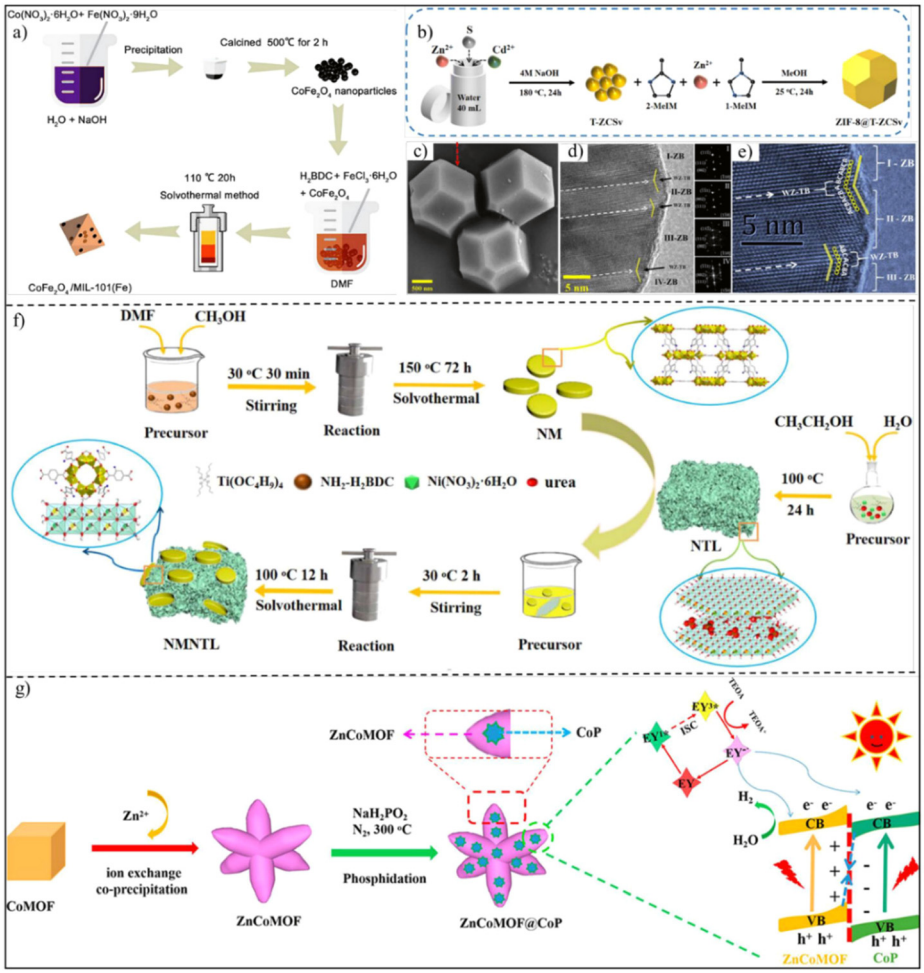

Fig. 7 (a) Scheme of the synthetic process of the $CuFe_2O_4$/MIL-101(Fe) heterojunction. Reprinted with permission from ref. 40. Copyright 2022 Elsevier. (b) Scheme showing the formation process. (c) SEM, (d) TEM and (e) HRTEM images of the ZIF-8@T-ZCSv heterojunction. Reprinted with permission from ref. 84. Copyright 2023 the Royal Society of Chemistry. (f) Diagram of the preparation route of NM, NTL and NMNTL. Reprinted with permission from ref. 41. Copyright 2023 the Royal Society of Chemistry. (g) Flow chart of the preparation of the ZnCoMOF@CoP S-scheme heterojunction. Reprinted with permission from ref. 86. Copyright 2022 American Chemical Society.

Different from COF materials, hydrogen-bonded organic frameworks (HOFs) self-assembled through hydrogen bonding have been rarely considered for photocatalytic applications due to their weak stability and low activity.[101,102] To address the problems, a typical Zr-based MOF, NH_2-UiO-66 (UiO), with high stability was selected as a support for coating a HOF, creating a MOF/HOF S-scheme heterojunction (Fig. 9d).[87] The amino groups on UiO permitted further functionalization with naphthalenetetracarboxylic dianhydride (NTCDA) through covalently bonding.

Subsequently, the heterogeneous nucleation and growth of a highly stable diamino triazole-type multi-site hydrogen-bonded HOF (DAT-HOF) were induced on the surface of the UiO host. As a result, NH_2-UiO-66@DAT-HOF (U@H2) core–shell hybrid materials were generated, as evidenced from the XRD pattern (Fig. 9e).

Among the diverse organic semiconductor materials, subphthalocyanines (SubPcs) are an uncommon type of coupled aromatic molecule. The solid tetrahedral structure and 14-π electron conjugation endows them with not only high response to visible light, but also superior photoelectric and thermal stability. On this basis, Ma *et al.* reported an H_{12}SubPcB-Br (SubPc-Br)/UiO-66 S-scheme heterojunction synthesized by a solvothermal route.[45] As seen in Fig. 9f, the supramolecular array of SubPc-Br was dynamically assembled with UiO-66 through the dynamic connection models of "B–O–Zr" and "cap" moieties. The Fourier transform infrared (FTIR) spectra (Fig. 9g) and high-resolution Br 3d XPS spectra (Fig. 9h) clearly demonstrated the formation of a SubPc-Br/UiO-66 heterojunction.

4.2 MOF-on-MOF heterojunction

The explosive expansion of the MOF field generates a distinctive class of MOF-on-MOF heterostructures by conjugating two or more different MOFs.[103] More importantly, when applying such a design for constructing MOF-on-MOF heterojunctions,

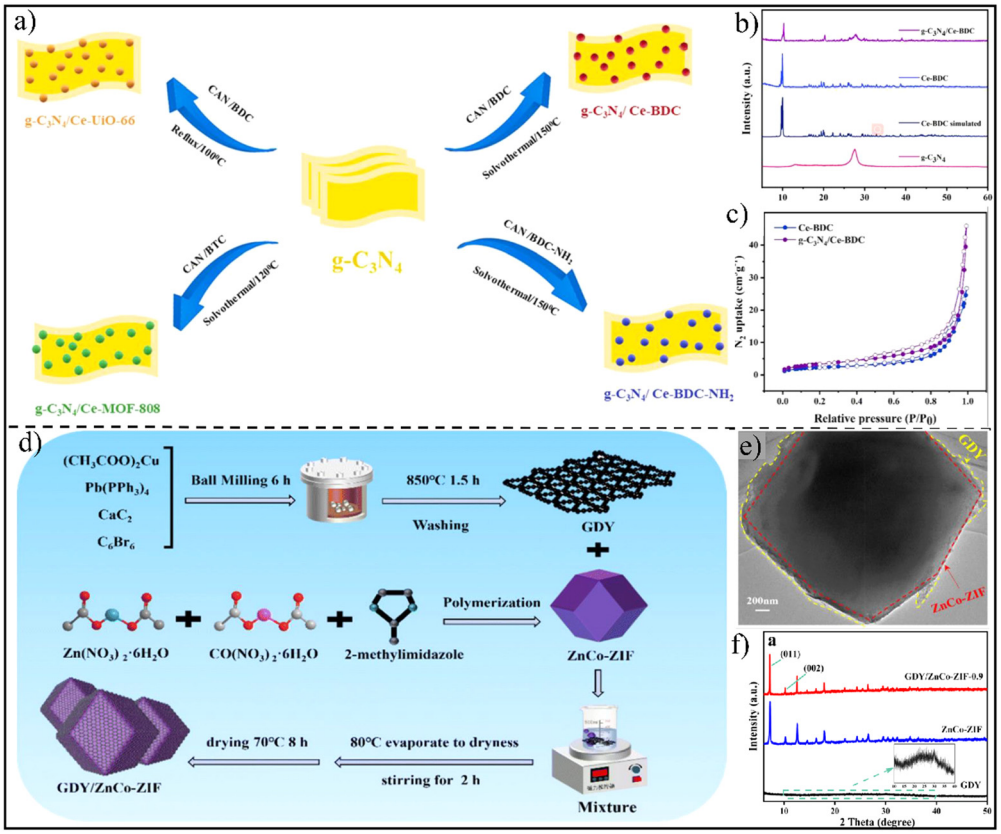

Fig. 8 (a) Synthesis process of g-C_3N_4/Ce-MOF. (b) XRD patterns of g-C_3N_4, Ce-BDC, and g-C_3N_4/Ce-BDC. (c) N_2 adsorption–desorption isotherms of Ce-BDC and g-C_3N_4/Ce-BDC. Reprinted with permission from ref. 43. Copyright 2023 Elsevier. (d) Schematic for the preparation of GDY/ZnCo-ZIF. (e) TEM image of GDY/ZnCo-ZIF. (f) XRD spectra of GDY, ZnCo-ZIF and GDY/ZnCo-ZIF. Reprinted with permission from ref. 96. Copyright 2023 Elsevier.

abundant interfacial chemical bonds can be formed *via* the interaction between exposed metals and/or ligands of the MOF units, which are highly conducive for electron transfer and charge separation, beyond the conventional MOF/non-MOF hybridization at a single MOF level to some extent.[37,104] A typical example is that the Yu and Liu group reported an MIL-125-NH_2@CoFe Prussian blue analogue (PBA) S-scheme heterojunction with a well-defined Ti–O–Co-bonded interface and an internal electric field.[44] Starting with MIL-125-NH_2 as the host material, an MIL-125-NH_2@ cobalt-based zeolite imidazole framework (ZIF-67) heterostructure was fabricated by selective deposition of ZIF-67 nanocrystals on the top and down surfaces of MIL-125-NH_2 cakes due to the facet-dependent electrostatic interaction. Afterwards, the MIL-125-NH_2@CoFe PBA heterojunction was generated *via* a ligand exchange treatment of MIL-125-NH_2@ZIF-67 in $[Fe(CN)_6]_3^-$ solution, where the ZIF-67 was selectively transformed into CoFe PBA (Fig. 10a). The scanning electron microscopy (SEM), transmission electron microscopy (TEM), high-angle annular dark-field scanning transmission electron microscopy (HAADF-STEM) and corresponding elemental mapping images (Fig. 10b–e) revealed a sandwich-like morphology of MIL-125-NH_2@CoFe PBA with hollow CoFe PBA nanocages selectively assembled on the top-down surfaces of MIL-125-NH_2 nanocakes. Fig. 10f and g show the synchrotron X-ray absorption fine structure (XAFS) profiles, verifying the formation of Ti–O–Co chemical bonds within the MOF-on-MOF heterojunction. As another example of MOF-on-MOF heterojunctions, a unique MIL-100(Fe)/NH_2-MIL-125(Ti) heterojunction was also prepared by a facile ball-milling approach.[105]

4.3 MOF derivative-based heterojunctions

As well as for direct use, MOFs are also ideal templates or precursors for the preparation of derived functional materials, such as carbon, metal compounds (*e.g.*, metal oxides,[106–108] metal sulfides,[109,110] metal phosphides[111,112]) and their composites, *via* thermal and/or chemical treatments. Compared with pristine MOFs, MOF derivatives usually possess higher chemical stability, stronger light harvesting and charge transfer ability, and thus have been considered a promising class of photocatalysts.[113,114] Naturally, the design of MOF-derived S-scheme heterojunctions has also witnessed great advances.[115,116] For example, S-scheme In_2O_3/ZnO nanotubes were synthesized by using In-MIL-68 as the precursor through a two-step annealing immersion process, as illustrated in Fig. 11a.[106] Also using MIL-68-derived In_2O_3 as a semi-

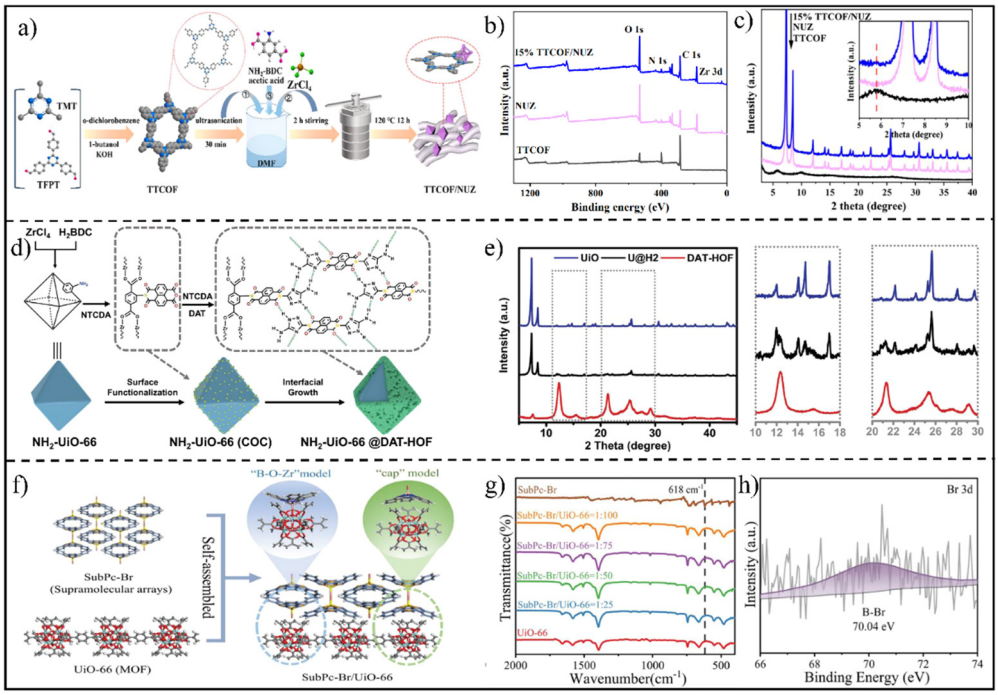

Fig. 9 (a) Illustration of the preparation of the TTCOF/NUZ composite. (b) XPS survey spectra and (c) PXRD patterns of TTCOF, NUZ and TTCOF/NUZ. Reprinted with permission from ref. 64. Copyright 2022 American Chemical Society. (d) Scheme presenting the synthetic procedure for NH_2-UiO-66@DAT-HOF photocatalysts. (e) XRD patterns of UiO, DAT-HOF, and the U@H2 hybrid. Reprinted with permission from ref. 87. Copyright 2022 Wiley-VCH. (f) Diagram of the synthesis of SubPc-Br/UiO-66. (g) FTIR spectra of the as-prepared samples. (h) High-resolution Br 3d XPS spectra of SubPc-Br/UiO-66. Reprinted with permission from ref. 45. Copyright 2023 Wiley-VCH.

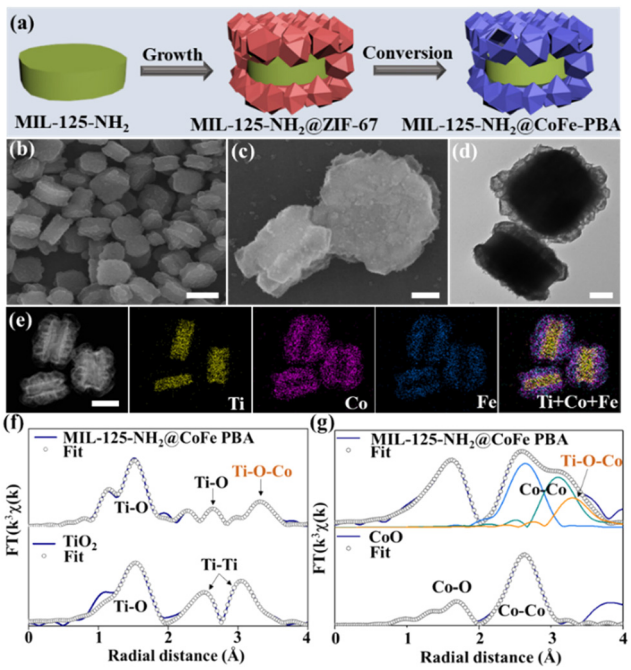

Fig. 10 (a) Illustration of the synthesis process of MIL-125-NH_2@CoFe PBA. (b and c) SEM, (d) TEM, (e) HAADF-STEM and the corresponding elemental mapping images. Scale bars are: (b), 1 μm; (e), 500 nm; and (c and d), 200 nm. (f) Ti coordination environments of MIL-125-NH_2@CoFe PBA and TiO_2 and (g) Co coordination environments of MIL-125-NH_2@CoFe PBA and CoO. Reprinted with permission from ref. 44. Copyright 2023 Wiley-VCH.

conductor, the interfacial growth of $CaIn_2S_4$, $MnIn_2S_4$ or $ZnIn_2S_4$ produced three kinds of S-scheme heterojunctions (Fig. 11b).[107]

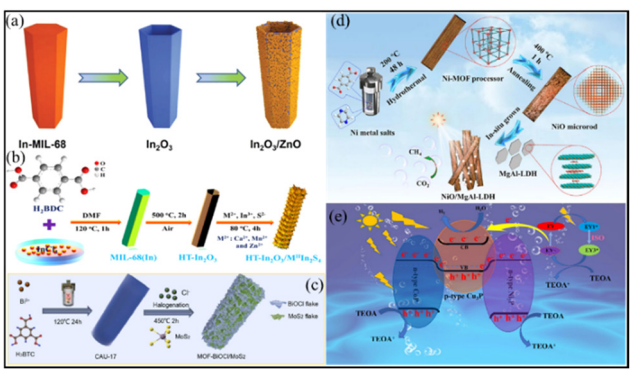

Fig. 11 (a) Schematic illustration of the preparation of tubular In_2O_3/ZnO heterostructures. Reprinted with permission from ref. 106. Copyright 2023 Wiley-VCH. (b) Schematic representation of the synthetic pathway of the HT-In_2O_3/MIIIIn_2S_4 (M = Ca, Mn, and Zn) heterostructure. Reprinted with permission from ref. 107. Copyright 2022 American Chemical Society. (c) Schematic illustration of the synthesis of MOF-BiOCl/MoS_2 composites. Reprinted with permission from ref. 117. Copyright 2022 Elsevier. (d) Schematic diagram of the fabrication process of NiO/MgAl-LDH photocatalysts. Reprinted with permission from ref. 108. Copyright 2023 Elsevier. (e) Illustration of the CoP/Cu_3P/Ni_2P S-scheme heterojunction. Reprinted with permission from ref. 112. Copyright 2022 American Chemical Society.

Additionally, through a sequential hydrothermal halogenation treatment, a 3D MOF-derived heterojunction assembled from BiOCl nanosheets and MoS_2 nanosheets was fabricated by using CAU-17 (CAU = Christian-Albrechts-Universität) as the Bi precursor (Fig. 11c).[117] In 2023, the Yang group developed a novel NiO/MgAl-LDH heterojunction photocatalyst in gas–solid mode by a two-step hydrothermal process (Fig. 11d). The heterojunction was composed of p-type NiO porous microrods derived from a Ni-MOF by calcination in air and n-type MgAl-LDH nanoplates *via in situ* growth on NiO.[108] Apart from metal oxides, MOF-derived metal phosphide-based S-scheme heterojunctions were also reported by Jin and coauthors recently (Fig. 11e). Furthermore, in their work, ZIF-67-derived CoP/Cu_3P/Ni_2P (CCNP) double S-scheme photocatalytic systems were constructed by simple hydrothermal and phosphating processes.[112]

5. Application of S-scheme heterojunction photocatalysts

5.1 Photocatalytic hydrogen evolution

H_2 as a clean fuel is expected to be an ideal alternative to fossil fuels in the future.[35,118] So far, various methods including steam reforming, electrolysis, hydrocarbon pyrolysis and photocatalysis have been reported to produce H_2.[119,120] Among them, the photocatalytic hydrogen evolution reaction (PHER) has gained significant attention, where the development of efficient photocatalysts is the central task.[121,122] Recently, MOF-based S-scheme heterojunctions have been applied in PHER with considerable success.[84,86,112] For instance, Jin *et al.* prepared a Co_3S_4/Mo_2S_3 S-scheme heterojunction for PHER *via*

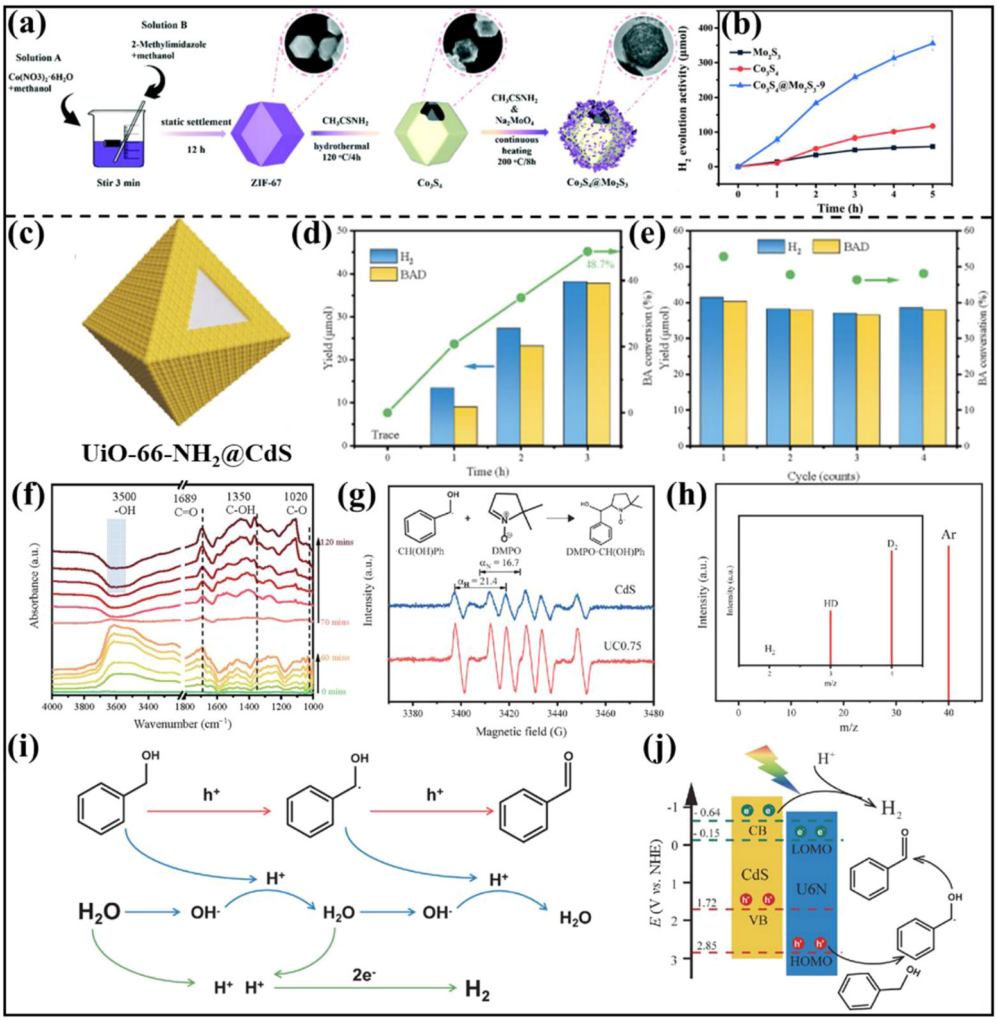

Fig. 12 (a) Schematic diagram of the preparation process of rhombic dodecahedral Co_3S_4@Mo_2S_3. (b) Hydrogen production activities of Co_3S_4, Mo_2S_3, Co_3S_4@Mo_2S_3-9. Reprinted with permission from ref. 109. Copyright 2022 Wiley-VCH. (c) Schematic of the UC composite. (d) Hourly photocatalytic performance. (e) Photocatalytic cycle test of the UC0.75 composite. (f) *In situ* DRIFTS spectra of the adsorbed BA aqueous solution on the UC0.75 composite under dark and irradiated conditions. (g) EPR spectra of CdS and the UC0.75 composite in CH_3CN solution (containing BA) with the addition of DMPO. (h) Mass spectrum of the gaseous products of PHER on UC0.75 using isotope-labelled D_2O and BA as reactants. (i and j) Reaction mechanism for photocatalytic BA conversion and H_2 evolution over the CdS/U6N S-scheme heterojunction. Reprinted with permission from ref. 81. Copyright 2022 Elsevier.

a stepwise hydrothermal method using ZIF-67 as the template (Fig. 12a).[109] Benefiting from the promoted charge transfer, the H_2 evolution amount of Co_3S_4@Mo_2S_3-9 (375.37 μmol) was about 7 and 3 times higher than those of pure Mo_2S_3 (53.85 μmol) and Co_3S_4 (114.44 μmol) (Fig. 12b).

To promote the simultaneous utilization of photogenerated electrons and holes, Xu and co-authors reported the synthesis of a UiO-66-NH_2 (U6N)/CdS S-scheme heterojunction (denoted as UC) (Fig. 12c) for efficient H_2 generation coupled with selective oxidation of benzyl alcohol (BA) under light irradiation.[81] After illumination for 3 h, the heterojunction with the optimized UiO-66-NH_2/CdS ratio (UC0.75) delivered a high H_2 production amount of 38.1 μmol and a benzaldehyde (BAD) yield of 37.8 μmol, superior to the single-component UiO-66-NH_2 and CdS (Fig. 12d). As well as high activity, UC0.75 also exhibited excellent photocatalytic stability with almost no performance decline after four consecutive cycles (Fig. 12e). *In situ* diffuse reflectance infrared Fourier transform spectroscopy (DRIFTS) was used to monitor the functional group changes in the adsorbed species on the surface of the photocatalyst during the photocatalytic reaction (Fig. 12f). The results showed that BA was dehydrogenated and oxidized into benzaldehyde (BAD) with the detection of a radical intermediate of $^{\bullet}$CH(OH)Ph (Fig. 12g). Using isotope-labelled heavy water (D_2O) and BA as reactants, the gaseous products were found to be mainly D_2 and HD, suggesting that the hydrogen protons in the coupling reaction system came from H_2O. Collectively, the reaction mechanism of photocatalytic H_2 production and coupled BA conversion to BAD over CdS/U6N heterojunction was depicted in Fig. 12i. Under illumination, the photogenerated holes located in U6N reacted first with benzyl alcohol to oxidize α-C on benzyl alcohol to produce $^{\bullet}$CH(OH)Ph, which was then converted to BAD by further oxidation. Meanwhile, the photogenerated electrons in CdS reduced the generated H^+ to form H_2 (Fig. 12j).

5.2 Photocatalytic CO_2 reduction

Photocatalytic CO_2 reduction for valuable chemical and fuel production is of great significance for achieving carbon neutrality goals. Nevertheless, the stable molecular structure of CO_2 with a high bonding energy of C=O bonds (750 kJ mol^{-1}) limits the practical application of photocatalytic CO_2 reduction.[47,49,123] To resolve the problem, Jing *et al.* synthesized a single-atom Ni@MOF/$BiVO_4$(Ni@MOF/BVO) S-scheme heterojunction. NTU-9 (NTU = Nanyang Technological University) with a 2D honeycomb structure was synthesized for immobilization of abundant single Ni(II) sites.[124]

The resulting Ni@MOF was coupled with BVO nanosheets by H-bonding-induced assembly, resulting in Ni@MOF/BVO 2D heterojunctions with wide-spectrum absorption (Fig. 13a). The photocatalytic performance for CO_2 reduction was assessed in pure water. By carefully altering the loading amounts of the MOF and Ni, the optimized sample produced the largest CO amount of 178 μmol g^{-1} with a CO selectivity of 99.2% and O_2 as the oxidative product. The CO_2 photoconversion is 66-fold that of the reference BVO nanoparticles. In contrast, the physically mixed sample without favourable interfacial bonding demonstrated negligible photoactivity enhancement compared with BVO. To avoid the interference of organic impurities, photoreduction of ^{13}C-labled CO_2 was further conducted over the Ni@6MOF/BVO photocatalyst. The gas chromatography-mass spectrum (Fig. 13c) showed peaks assigned to $^{13}CH_4$ and ^{13}CO, indicating that the products were evolved from the photoreduction of $^{13}CO_2$. Under UV-vis light irradiation, the photoelectrons could transfer from BVO to the MOF and then directionally to single Ni(II) sites. The holes of BVO would oxidize water to produce O_2 and the electrons would reduce the adsorbed CO_2 by single Ni atoms along with vicinal hydroxyl groups to produce CO (Fig. 13d).

5.3 C–H functionalization

Photocatalysis driven C–H functionalization is an important direction in organic synthesis toward heterocyclic compounds.[125,126] Very recently, a MOF-based S-scheme heterojunction was applied for activating C–H bonds with superior performance by Yu and colleagues.[46] In their work, S-scheme heterojunctions composed of titanium–organic frameworks, MOF-902@thiophene-based covalent triazine

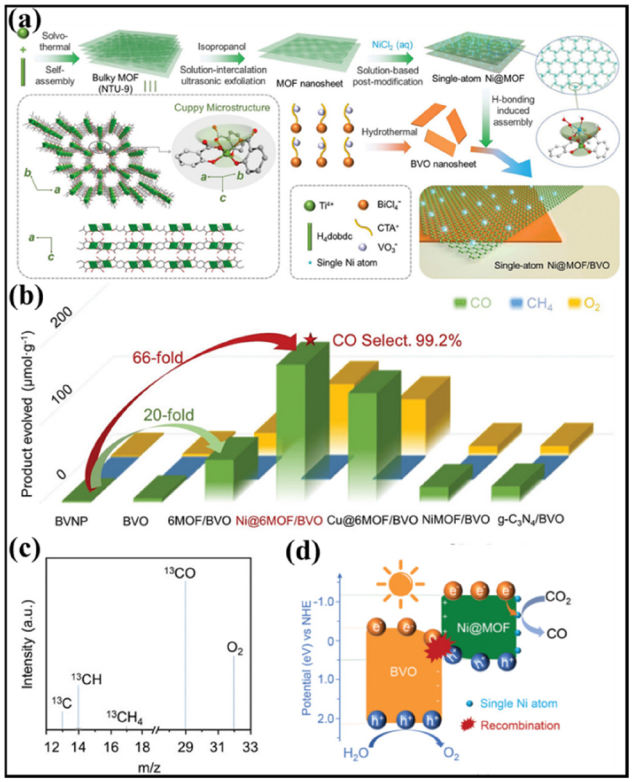

Fig. 13 (a) Synthetic illustration of the single-atom Ni@MOF/BVO heterojunction photocatalyst. (b) Photoactivities of BVNP, BVO, 6MOF/BVO, Ni@6MOF/BVO, Cu@6MOF/BVO, NiMOF/BVO, and g-C_3N_4/BVO for CO_2 reduction. (c) Mass spectrum of the products over Ni@6MOF/BVO in the photocatalytic reduction of $^{13}CO_2$. (d) Illustration of the proposed photocatalytic mechanism of Ni@6MOF/BVO based on S-scheme charge transfer for CO_2 conversion under UV-vis light irradiation. Reprinted with permission from ref. 124. Copyright 2022 Wiley-VCH.

frameworks (CTF-Th), were synthesized by growth of MOF-902 on preformed CTF-Th (Fig. 14a). The obtained heterojunction exhibited interfacial Ti–S bonds and controllable oxygen vacancies (OVs). The MOF-902@CTF-Th$_{1.5}$ heterojunction with a MOF-902@CTF-Th mass ratio of 1.5 was identified as the optimal sample, showing the highest efficiency of 98% in the photocatalytic C3-acylation of indoles. The product yield was calculated to be 8.2 times larger than that of pristine CTF-Th or MOF-902 (Fig. 14b). Furthermore, the constructed platform was versatile, which could extend the scope of substrates to 15 different examples. The origin of the excellent performance was ascribed to the enhanced interfacial charge separation and transfer by introducing Ti–S bonds and moderate OVs. This promoted the activation of molecular oxygen into $^{\bullet}O_2^-$ and $_1O^2$ by photogenerated electrons, which accounted for the formation of targeted 3-benzoylindole by their reaction with phenylglyoxylic acid and indole (Fig. 14c).

5.4 H_2O_2 production

Hydrogen peroxide (H_2O_2), as a green oxidant, plays irreplaceable roles in various important applications.[127–130] The photocatalytic two-electron oxygen reduction reaction (2e-ORR) has recently emerged as a promising alternative route to the traditional anthraquinone oxidation process.[131,132] To date, great efforts have been devoted to designing high-performance 2e-ORR photocatalysts, however, the investigation of MOF-based S-scheme heterojunctions for H_2O_2 production is rare.

As a typical example, the Yu group reported an S-scheme heterojunction by coupling MIL-125-NH$_2$-derived TiO_2 and an organic semiconductor, resorcinol–formaldehyde (RF) resin.[133] Notably, two types of core–shell TiO_2@RF and RF@TiO_2 photocatalysts were prepared with TiO_2 nanocrystals deposited on the interior and exterior surfaces of a hollow RF shell, respectively, to study the impact of spatial arrangement (Fig. 15a). When used as a 2e-ORR photocatalyst for H_2O_2 production, the TiO_2@RF heterojunction delivered a high H_2O_2 yield of 66.6 mM g^{-1} h^{-1} in pure water, significantly outperforming single RF, TiO_2 and the RF@TiO_2 counterpart (Fig. 15b, c and d). The possible reason for the enhanced performance of TiO_2@RF may be ascribed to the design of S-scheme heterojunctions with a specific spatial configuration, enabling maximally preserved redox ability, promoted charge separation and active site exposure, and restricted H_2O_2 decomposition.

5.5 Wastewater treatment

As well as producing valuable chemicals, photocatalysis also affords an efficient route for wastewater treatment.[134–136] Compared to single-component semiconductors, S-scheme heterojunctions usually exhibited higher activity for pollutant degradation.[44,82,137,138] For instance, Neppolian *et al.* devel-

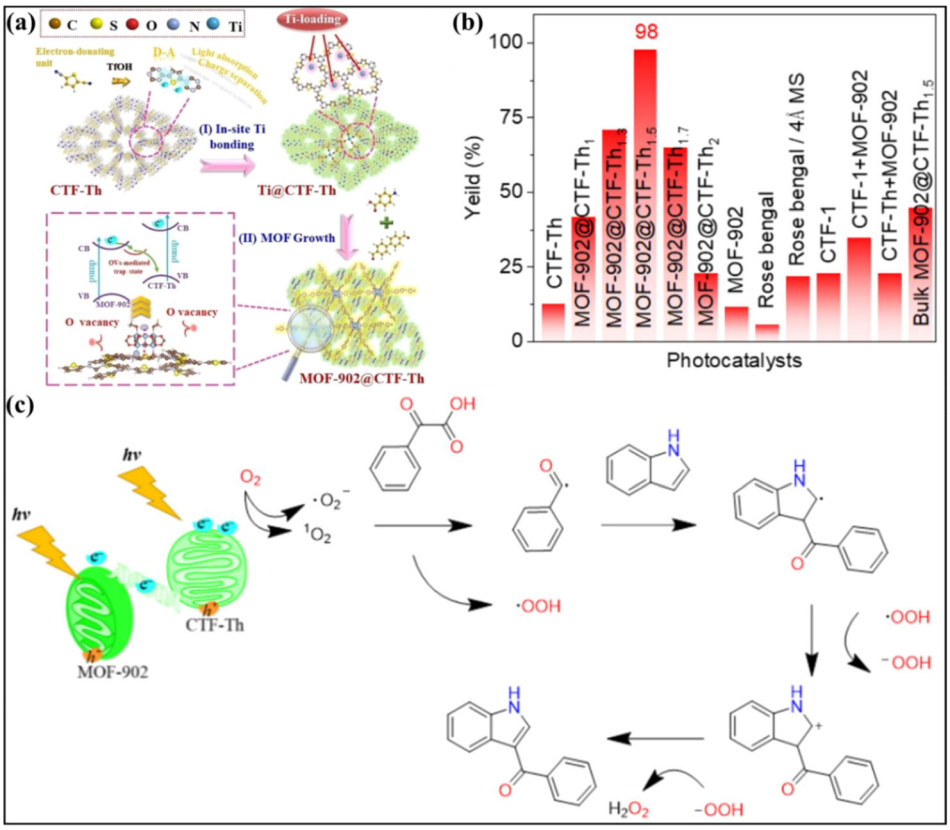

Fig. 14 (a) Schematic presentation of the synthetic route of the MOF-902@CTF-Th heterostructure. (b) Decarboxylative C3-acylation of indoles of different photocatalysts. (c) Proposed reaction mechanism for decarboxylative C3-acylation of indoles in the presence of the MOF-902@CTF-Th photocatalyst. Reprinted with permission from ref. 46. Copyright 2023 Wiley-VCH.

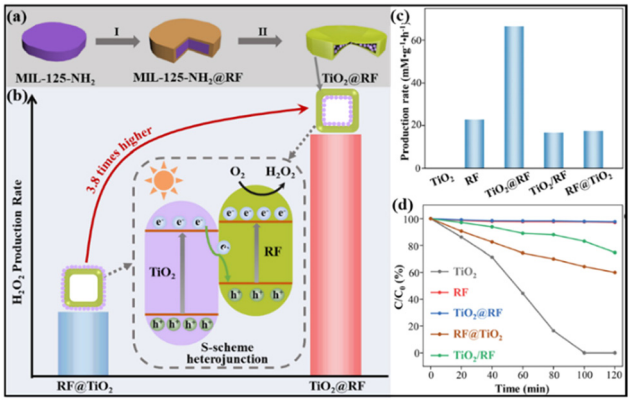

Fig. 15 Illustration of (a) the synthesis of the TiO_2@RF S-scheme heterostructure and (b) H_2O_2 production rates of TiO_2@RF and RF@TiO_2 photocatalysts with reversed spatial arrangements. (c) H_2O_2 production rates and (d) photocatalytic H_2O_2 decomposition rates over TiO_2@RF, RF@TiO_2, RF, TiO_2, and TiO_2/RF. Reprinted with permission from ref. 133. Copyright 2023 Wiley-VCH.

oped a Cu-BTC (a copper-based MOF)@$ZnWO_4$ S-scheme heterojunction *via* an ultrasound-assisted hydrothermal strategy.[138] Under simultaneous visible-light irradiation and ultrasound conditions, the Cu-BTC/$ZnWO_4$ heterojunction completely removed the tetracycline (TC, a typical type of antibiotic) within 60 min (Fig. 16a). The kinetic constant value of the Cu-BTC/$ZnWO_4$ heterojunction was estimated to be 0.04908 min^{-1}, much higher than those of Cu-BTC

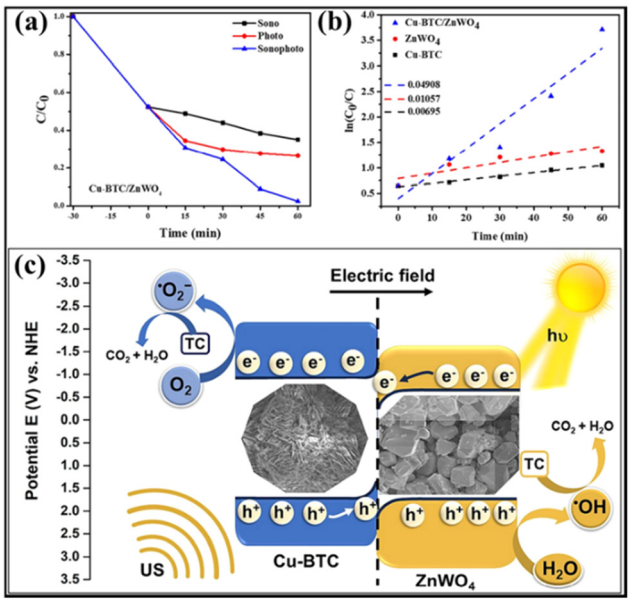

Fig. 16 (a) Analysis of Cu-BTC/$ZnWO_4$ using C/C_0 plots for sono-, photo-, and sonophotocatalytic processes. (b) Kinetic studies of Cu-BTC, $ZnWO_4$, and Cu-BTC/$ZnWO_4$. (c) Schematic illustration depicting the degradation of TC using sonophotocatalysis on Cu-BTC/$ZnWO_4$ S-scheme photocatalysts. Reprinted with permission from ref. 138. Copyright 2023 Elsevier.

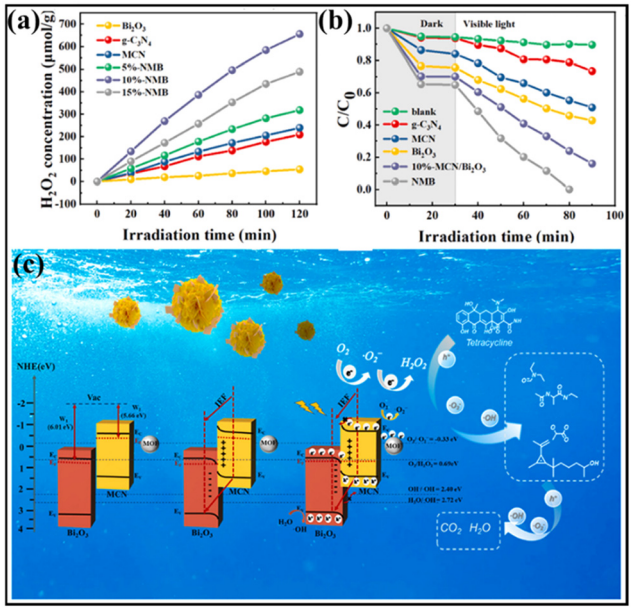

Fig. 17 (a) Degradation performance of TC using various photocatalysts. (b) H_2O_2 production performances of different photocatalysts. (c) Illustration of the proposed photocatalytic mechanism of 10%-NMB based on S-scheme charge transfer for the degradation of TC. Reprinted with permission from ref. 139. Copyright 2023 Elsevier.

(0.00695 min^{-1}) and $ZnWO_4$ (0.01057 min^{-1}), indicating the superior sonophotocatalytic activity of the Cu-BTC/$ZnWO_4$ heterojunction ascribed to the S-scheme charge transfer (Fig. 16b and c).

Different from the aforementioned TC degradation process with the aid of sonication, Bao and co-workers reported the simultaneous TC removal and H_2O_2 production over an S-type heterojunction, which was synthesized by growing Bi_2O_3 nanocrystals and NH_2-MIL-101 (an iron-based MOF) onto surface-modified g-C_3N_4 (the resulting heterojunction was named NMB).[139] As shown in Fig. 17a, the H_2O_2 generation amount of the optimized sample 10%-NMB reached 655.63 μmol g^{-1} after light irradiation for 120 min in the absence of TC, outperforming those of Bi_2O_3 and the NH_2-MIL-101(Fe)/C_3N_4 composite. Moreover, the TC degradation efficiency of the photocatalysts was further explored. As can be seen, the ternary 10%-NMB demonstrated the highest photocatalytic activity with 100% degradation of TC within 50 min (Fig. 17b and c).

6. Conclusions and outlook

In summary, MOFs as an important family of porous crystalline materials have demonstrated outstanding performances in many fields.[14] However, their photocatalytic performance has been seriously restricted by their relatively weak light absorption capacity, rapid recombination of photogenerated charges and limited redox ability. Construction of MOF-based S-scheme heterojunction photocatalysts provides an efficient strategy to enhance the light harvesting ability, improve the

electron–hole separation efficiency and maximize the redox capability, endowing MOFs with improved photocatalytic properties. This work reviews the latest progress of MOF-based S-scheme photocatalysts with respect to their synthesis, structures and applications. Although significant advances have been achieved in this emerging field, there are still several challenges for further investigations.

Firstly, from a morphological aspect, most of the reported MOF-based photocatalysts exhibited a micropore-dominated structure, preventing the active site accessibility and mass transfer. To address these problems, introducing hierarchical pores (*e.g.* mesopores and macropores) or construction of complex architectures (*e.g.* hollow or open-frame-like structures) in MOF-based semiconductors is feasible.[140–142] In this regard, synthetic strategies including selective etching, defect engineering and template methods are suggested.[82,143,144]

Secondly, compared to the huge number of reported semiconducting materials, those used for preparing MOF-based S-scheme heterojunctions are limited. The involved materials are mainly metal oxides, metal sulphides or carbon-based materials. Further incorporation of other promising photocatalysts such as metal nitrides,[145,146] bismuth oxyhalides[147,148] and metal selenides[149,150] will undoubtedly offer new opportunities for developing efficient MOF-based S-scheme heterojunctions. Beyond MOF/non-MOF combinations, the design of MOF-on-MOF heterojunctions is expected to demonstrate additional merits as mentioned before, while has been rarely studied.

Finally, from the application perspective, an in-depth understanding of the underlying structure–performance relationship of MOF-based S-scheme heterojunctions is highly desired. *In situ* characterization methods such as Raman spectroscopy, infrared spectroscopy, XRD, XPS and TEM can serve as powerful tools for monitoring the composition and structure evolution of the photocatalysts during photochemical processes. Besides, to fully implement the MOF-based S-scheme heterojunctions, the simultaneous utilization of photogenerated holes and electrons for the coupled redox reaction toward high-value chemical production is of great significance.[151,152] Moreover, microporosity as one of the most important features of MOFs determines the reactant transport during photocatalysis. Therefore, the investigation of the pore connectivity throughout the interface between different materials is a crucial issue, which has rarely been reported. Another crucial step for their practical application is constructing MOF-based S-scheme heterojunctions at the macroscopic scale with the forms of gel, film or membrane.[153,154]

It is believed that the further expansion of MOF-based S-scheme heterojunction photocatalysts from the above directions will promote the application of photocatalysis technology in various important fields.

Conflicts of interest

There are no conflicts to declare.

Acknowledgements

The authors acknowledge the support from the National Natural Science Foundation of China (NSFC 51908218 and 21905092), the Scientific Research Foundation of Shanghai Institute of Technology (10120K226156-A06-YJ2022-62), the Shanghai Higher Education Institution Young Teacher Training Funding Program (ZZ202312031) and the Key Laboratory of Jiangsu Province for Chemical Pollution Control and Resources Reuse (Nanjing University of Science and Technology).

References

1 N. Keller, J. Ivanez, J. Highfield and A. M. Ruppert, *Appl. Catal., B*, 2021, **296**, 120320.
2 L. Lu, M. Sun, T. Wu, Q. Lu, B. Chen, C. H. Chan, H. H. Wong and B. Huang, *Small Methods*, 2023, **7**, 2300430.
3 B. Zhu, J. Sun, Y. Zhao, L. Zhang and J. Yu, *Adv. Mater.*, 2023, 2310600.
4 Y. Song, X. Zheng, Y. Yang, Y. Liu, J. Li, D. Wu, W. Liu, Y. Shen and X. Tian, *Adv. Mater.*, 2023, 2305835.
5 L. Wang, X. Zheng, L. Chen, Y. Xiong and H. Xu, *Angew. Chem., Int. Ed.*, 2018, **57**, 3454–3458.
6 X. Ruan, S. Li, C. Huang, W. Zheng, X. Cui and S. K. Ravi, *Adv. Mater.*, 2023, 2305285.
7 C. Foo, Y. Li, K. Lebedev, T. Chen, S. Day, C. Tang and S. C. E. Tsang, *Nat. Commun.*, 2021, **12**, 661.
8 Z. Wei, S. Zhao, W. Li, X. Zhao, C. Chen, D. L. Phillips, Y. Zhu and W. Choi, *ACS Catal.*, 2022, **12**, 11436–11443.
9 X. Zheng, Y. Song, Y. Liu, Y. Yang, D. Wu, Y. Yang, S. Feng, J. Li, W. Liu, Y. Shen and X. Tian, *Coord. Chem. Rev.*, 2023, **475**, 214898.
10 Y. Wang, S. Wang and X. W. Lou, *Angew. Chem., Int. Ed.*, 2019, **58**, 17236–17240.
11 G. Yan, X. Sun, K. Zhang, Y. Zhang, H. Li, Y. Dou, D. Yuan, H. Huang, B. Jia, H. Li and T. Ma, *Small*, 2022, **18**, 2201340.
12 X. Chen and K. M. Ok, *Chem. Sci.*, 2022, **13**, 3942–3956.
13 X. Feng, R. Zheng, C. Gao, W. Wei, J. Peng, R. Wang, S. Yang, W. Zou, X. Wu, Y. Ji and H. Chen, *Nat. Commun.*, 2022, **13**, 2146.
14 F. He, Y. Lu, Y. Wu, S. Wang, Y. Zhang, P. Dong, Y. Wang, C. Zhao, S. Wang, J. Zhang and S. Wang, *Adv. Mater.*, 2023, 2307490.
15 L. Sun, D. Wang, Y. Li, B. Wu, Q. Li, C. Wang, S. Wang and B. Jiang, *Chin. Chem. Lett.*, 2023, **34**, 107490.
16 M. Traxler, S. Gisbertz, P. Pachfule, J. Schmidt, J. Roeser, S. Reischauer, J. Rabeah, B. Pieber and A. Thomas, *Angew. Chem., Int. Ed.*, 2022, **61**, e202117738.
17 C. Wu, X. Li, M. Shao, J. Kan, G. Wang, Y. Geng and Y. B. Dong, *Chin. Chem. Lett.*, 2022, **33**, 4559–4562.
18 A. Dhakshinamoorthy, A. M. Asiri and H. García, *Angew. Chem., Int. Ed.*, 2016, **55**, 5414–5445.

19 J. Chen, R. Abazari, K. A. Adegoke, N. W. Maxakato, O. S. Bello, M. Tahir, S. Tasleem, S. Sanati, A. M. Kirillov and Y. Zhou, *Coord. Chem. Rev.*, 2022, **469**, 214664.
20 C. Liu, J. Wang, J. Wan and C. Yu, *Coord. Chem. Rev.*, 2021, **432**, 213743.
21 Y. Li, Y. Wei, W. He, Z. Tang, J. Xiong and Z. Zhao, *Chin. Chem. Lett.*, 2023, **34**, 108417.
22 L. Jiao and H. L. Jiang, *Chin. J. Catal.*, 2023, **45**, 1–5.
23 H. Sepehrmansourie, H. Alamgholiloo, N. Noroozi Pesyan and M. A. Zolfigol, *Appl. Catal., B*, 2023, **321**, 122082.
24 C. Zhang, C. Xie, Y. Gao, X. Tao, C. Ding, F. Fan and H. L. Jiang, *Angew. Chem., Int. Ed.*, 2022, **61**, e202204108.
25 N. Y. Huang, Y. T. Zheng, D. Chen, Z. Y. Chen, C. Z. Huang and Q. Xu, *Chem. Soc. Rev.*, 2023, **52**, 7949–8004.
26 Z. Jiang, X. Xu, Y. Ma, H. S. Cho, D. Ding, C. Wang, J. Wu, P. Oleynikov, M. Jia, J. Cheng, Y. Zhou, O. Terasaki, T. Peng, L. Zan and H. Deng, *Nature*, 2020, **586**, 549–554.
27 X. Gong, Y. Shu, Z. Jiang, L. Lu, X. Xu, C. Wang and H. Deng, *Angew. Chem., Int. Ed.*, 2020, **59**, 5326–5331.
28 J. Xiao, R. Li and H. Jiang, *Small Methods*, 2023, **7**, 2201258.
29 L. Sun, Y. Yuan, F. Wang, Y. Zhao, W. Zhan and X. J. N. E. Han, *Nano Energy*, 2020, **74**, 104909.
30 L. Liu, S. Du, X. Guo, Y. Xiao, Z. Yin, N. Yang, Y. Bao, X. Zhu, S. Jin and Z. Feng, *J. Am. Chem. Soc.*, 2022, **144**, 2747–2754.
31 M. Li, X. Liu, Y. Che, H. Xing, F. Sun, W. Zhou and G. Zhu, *Angew. Chem., Int. Ed.*, 2023, **62**, e202308651.
32 S. Navalón, A. Dhakshinamoorthy, M. Álvaro, B. Ferrer and H. García, *Chem. Rev.*, 2023, **123**, 445–490.
33 Y. Qian, F. Zhang and H. Pang, *Adv. Funct. Mater.*, 2021, **31**, 2104231.
34 Y. Li, J. Zhang, Q. Chen, X. Xia and M. Chen, *Adv. Mater.*, 2021, **33**, 2100855.
35 C. Liu, Q. Sun, L. Lin, J. Wang, C. Zhang, C. Xia, T. Bao, J. Wan, R. Huang, J. Zou and C. Yu, *Nat. Commun.*, 2020, **11**, 4971.
36 H. Peng, J. Raya, F. Richard, W. Baaziz, O. Ersen, A. Ciesielski and P. Samorì, *Angew. Chem., Int. Ed.*, 2020, **59**, 19602–19609.
37 W. Han, L. H. Shao, X. J. Sun, Y. H. Liu, F. M. Zhang, Y. Wang, P. Y. Dong and G. L. Zhang, *Appl. Catal., B*, 2022, **317**, 121710.
38 J. Wang, Y. Mao, R. Zhang, Y. Zeng, C. Li, B. Zhang, J. Zhu, J. Ji, D. Liu and R. Gao, *Adv. Sci.*, 2022, **9**, 2204036.
39 H. Yang, C. Yang, N. Zhang, K. Mo, Q. Li, K. Lv, J. Fan and L. Wen, *Appl. Catal., B*, 2021, **285**, 119801.
40 W. Shi, Y. Fu, H. Sun, X. Sun, C. Hao, F. Guo and Y. Tang, *Inorg. Chem. Commun.*, 2022, **146**, 110140.
41 R. Wang, Z. Wang, X. Shang, Y. Yang, J. Ding and Q. Zhong, *J. Mater. Chem. A*, 2023, **11**, 630–641.
42 Z. Jin, Y. Li and Q. Ma, *Trans. Tianjin Univ.*, 2021, **27**, 127–138.
43 M. D. Goudarzi, N. Khosroshahi, A. Hamlehdar and V. Safarifard, *J. Environ. Chem. Eng.*, 2023, **11**, 110169.
44 L. Yuan, C. Zhang, Y. Zou, T. Bao, J. Wang, C. Tang, A. Du, C. Yu and C. Liu, *Adv. Funct. Mater.*, 2023, 2214627.
45 Z. Zheng, B. Wang, Z. Li, H. Hao, C. Wei, W. Luo, L. Jiao, S. Zhang, B. Zhou and X. Ma, *Small*, 2023, 2306820.
46 Z. Gao, Y. Jian, S. Yang, Q. Xie, C. J. Ross Mcfadzean, B. Wei, J. Tang, J. Yuan, C. Pan and G. Yu, *Angew. Chem., Int. Ed.*, 2023, e202304173.
47 L. Zhang, J. Zhang, H. Yu and J. Yu, *Adv. Mater.*, 2022, **34**, 2107668.
48 Q. Xu, L. Zhang, B. Cheng, J. Fan and J. Yu, *Chem*, 2020, **6**, 1543–1559.
49 L. Wang, B. Zhu, J. Zhang, J. B. Ghasemi, M. Mousavi and J. Yu, *Matter*, 2022, **5**, 4187–4211.
50 J. Low, J. Yu, M. Jaroniec, S. Wageh and A. A. Al-Ghamdi, *Adv. Mater.*, 2017, **29**, 1601694.
51 H. Zhou, Y. Qu, T. Zeid and X. Duan, *Energy Environ. Sci.*, 2012, **5**, 6732–6743.
52 H. Wang, L. Zhang, Z. Chen, J. Hu, S. Li, Z. Wang, J. Liu and X. Wang, *Chem. Soc. Rev.*, 2014, **43**, 5234–5244.
53 C. Xu, P. Ravi Anusuyadevi, C. Aymonier, R. Luque and S. Marre, *Chem. Soc. Rev.*, 2019, **48**, 3868–3902.
54 P. Zhou, J. Yu and M. Jaroniec, *Adv. Mater.*, 2014, **26**, 4920–4935.
55 H. Tada, T. Mitsui, T. Kiyonaga, T. Akita and K. Tanaka, *Nat. Mater.*, 2006, **5**, 782–786.
56 X. Li, C. Garlisi, Q. Guan, S. Anwer, K. Al-Ali, G. Palmisano and L. Zheng, *Mater. Today*, 2021, **47**, 75–107.
57 J. Low, C. Jiang, B. Cheng, S. Wageh, A. A. Al-Ghamdi and J. Yu, *Small Methods*, 2017, **1**, 5.
58 B. J. Ng, L. K. Putri, X. Y. Kong, Y. W. Teh, P. Pasbakhsh and S. P. Chai, *Adv. Sci.*, 2020, **7**, 7.
59 S. T. Kochuveedu, Y. H. Jang and D. H. Kim, *Chem. Soc. Rev.*, 2013, **42**, 8467–8493.
60 K. E. Byun, H. J. Chung, J. Lee, H. Yang, H. J. Song, J. Heo, D. H. Seo, S. Park, S. W. Hwang, I. Yoo and K. Kim, *Nano Lett.*, 2013, **13**, 4001–4005.
61 F. Ou, D. B. Buchholz, F. Yi, B. Liu, C. Hseih, R. P. H. Chang and S. T. Ho, *ACS Appl. Mater. Interfaces*, 2011, **3**, 1341–1345.
62 P. Hao, Z. Chen, Y. Yan, W. Shi and F. Guo, *Sep. Purif. Technol.*, 2024, **330**, 125302.
63 F. He, B. Zhu, B. Cheng, J. Yu, W. Ho and W. Macyk, *Appl. Catal., B*, 2020, **272**, 119006.
64 Q. Niu, S. Dong, J. Tian, G. Huang, J. Bi and L. Wu, *ACS Appl. Mater. Interfaces*, 2022, **14**, 24299–24308.
65 T. Li, N. Tsubaki and Z. Jin, *J. Mater. Sci. Technol.*, 2024, **169**, 82–104.
66 P. Hu, G. Liang, B. Zhu, W. Macyk, J. Yu and F. Xu, *ACS Catal.*, 2023, **13**, 12623–12633.
67 C. Cheng, B. He, J. Fan, B. Cheng, S. Cao and J. Yu, *Adv. Mater.*, 2021, **33**, 2100317.
68 P. Chang, Y. Wang, Y. Wang and Y. J. Zhu, *Chem. Eng. J.*, 2022, **450**, 137804.
69 B. Xia, B. He, J. Zhang, L. Li, Y. Zhang, J. Yu, J. Ran and S. Z. Qiao, *Adv. Energy Mater.*, 2022, **12**, 2201449.

70 Y. Huang, F. Mei, J. Zhang, K. Dai and G. Dawson, *Acta Phys.-Chim. Sin.*, 2022, **38**, 2108028.
71 F. Li, G. Zhu, J. Jiang, L. Yang, F. Deng and X. Li, *J. Mater. Sci. Technol.*, 2023, **177**, 142–180.
72 X. Chen, R. Guo, W. Pan, Y. Yuan, X. Hu, Z. Bi and J. Wang, *Appl. Catal., B*, 2022, **318**, 121839.
73 L. Wang, X. Fei, L. Zhang, J. Yu, B. Cheng and Y. Ma, *J. Mater. Sci. Technol.*, 2022, **112**, 1–10.
74 S. Li, M. Cai, C. Wang, Y. Liu, N. Li, P. Zhang and X. Li, *J. Mater. Sci. Technol.*, 2022, **123**, 177–190.
75 F. Li, X. Li, S. Tong, J. Wu, T. Zhou, Y. Liu and J. Zhang, *Nano Energy*, 2023, **117**, 108849.
76 X. Wang, M. Sayed, O. Ruzimuradov, J. Zhang, Y. Fan, X. Li, X. Bai and J. Low, *Appl. Mater. Today*, 2022, **29**, 101609.
77 J. Tian, Y. Sang, Z. Zhao, W. Zhou, D. Wang, X. Kang, H. Liu, J. Wang, S. Chen, H. Cai and H. Huang, *Small*, 2013, **9**, 3864–3872.
78 M. Sayed, B. Zhu, P. Kuang, X. Liu, B. Cheng, A. A. A. Ghamdi, S. Wageh, L. Zhang and J. Yu, *Adv. Sustainable Syst.*, 2022, **6**, 2100264.
79 H. Ren, F. Qi, A. Labidi, J. Zhao, H. Wang, Y. Xin, J. Luo and C. Wang, *Appl. Catal., B*, 2023, **330**, 122587.
80 H. Yang, L. Jia, Q. Zhang, S. Yuan, T. Ohno and B. J. S. Xu, *Small*, 2023, 2308743.
81 B. Liu, J. Cai, J. Zhang, H. Tan, B. Cheng and J. Xu, *Chin. J. Catal.*, 2023, **51**, 204–215.
82 J. Wei, Y. Chen, H. Zhang, Z. Zhuang and Y. J. Yu, *Chin. J. Catal.*, 2021, **42**, 78–86.
83 J. Sun, Y. Guan, G. Yang, S. Qiu, H. Shao, Y. Wang, G. Li and S. Xiao, *ACS Sustainable Chem. Eng.*, 2023, **11**, 14827–14840.
84 Y. Zhang, D. Lu, Z. Wang, M. Zhou, K. K. Kondamareddy, J. Li, H. Fan, D. Cao and W. Ho, *Inorg. Chem. Front.*, 2023, **10**, 6683–6700.
85 C. Luo, Y. Lin, Y. Zhang, S. Zhang, S. Tong, S. Wu and C. Yang, *Sep. Purif. Technol.*, 2023, **320**, 124052.
86 Y. Quan, G. Wang, X. Wang, X. Guo, X. Hao, K. Wang and Z. Jin, *Langmuir*, 2022, **38**, 12617–12629.
87 J. Wang, Y. Mao, R. Zhang, Y. Zeng, C. Li, B. Zhang, J. Zhu, J. Ji, D. Liu, R. Gao and Y. Ma, *Adv. Sci.*, 2022, **9**, 2204036.
88 M. R. Patel and S. K. Kailasa, *ChemistrySelect*, 2022, **7**, e202201849.
89 Y. Wang, R. Zhang, Z. Zhang, J. Cao and T. Ma, *Adv. Mater. Interfaces*, 2019, **6**, 1901429.
90 J. Fu, J. Yu, C. Jiang and B. Cheng, *Adv. Energy Mater.*, 2018, **8**, 1701503.
91 S. K. Gaddam, R. Pothu and R. Boddula, *Polym. Compos.*, 2020, **41**, 430–442.
92 J. Li, L. Zhu, C. H. Tung and L. Z. Wu, *Angew. Chem., Int. Ed.*, 2023, **62**, e202301384.
93 Y. Y. Han, X. L. Lu, S. F. Tang, X. P. Yin, Z. W. Wei and T. B. Lu, *Adv. Energy Mater.*, 2018, **8**, 1702992.
94 C. Wang, X. Han, Q. Xu, Y. N. Sun, J. Arbiol, M. N. Ghazzal and J. Li, *J. Mater. Chem. A*, 2023, **11**, 3380–3387.
95 Y. Wang, R. Hu, Y. Li, F. Wang, J. Shang and J. Shui, *Nano Res.*, 2022, **15**, 1054–1060.
96 K. Wang, X. Kong, H. Xie, S. Li, M. Wang and Z. Jin, *Dalton Trans.*, 2023, **52**, 8716–8727.
97 H. Wang, H. Wang, Z. Wang, L. Tang, G. Zeng, P. Xu, M. Chen, T. Xiong, C. Zhou, X. Li, D. Huang, Y. Zhu, Z. Wang and J. Tang, *Chem. Soc. Rev.*, 2020, **49**, 4135–4165.
98 A. P. Côté, A. I. Benin, N. W. Ockwig, M. O'Keeffe, A. J. Matzger and O. M. Yaghi, *Science*, 2005, **310**, 1166–1170.
99 Y. Zhang, H. Liu, F. Gao, X. Tan, Y. Cai, B. Hu, Q. Huang, M. Fang and X. Wang, *EnergyChem*, 2022, **4**, 100078.
100 R. Freund, O. Zaremba, G. Arnauts, R. Ameloot, G. Skorupskii, M. Dincă, A. Bavykina, J. Gascon, A. Ejsmont, J. Goscianska, M. Kalmutzki, U. Lächelt, E. Ploetz, C. S. Diercks and S. Wuttke, *Angew. Chem., Int. Ed.*, 2021, **60**, 23975–24001.
101 R. B. Lin, Y. He, P. Li, H. Wang, W. Zhou and B. Chen, *Chem. Soc. Rev.*, 2019, **48**, 1362–1389.
102 I. Hisaki, Y. Suzuki, E. Gomez, Q. Ji, N. Tohnai, T. Nakamura and A. Douhal, *J. Am. Chem. Soc.*, 2019, **141**, 2111–2121.
103 L. Mao and J. Qian, *Small*, 2023, 2308732.
104 C. Liu, L. Lin, Q. Sun, J. Wang, R. Huang, W. Chen, S. Li, J. Wan, J. Zou and C. Yu, *Chem. Sci.*, 2020, **11**, 3680–3686.
105 L. Wang, K. Zhang, J. Qian, M. Qiu, N. Li, H. Du, X. Hu, Y. Fu, M. Tan, D. Hao and Q. Wang, *Chemosphere*, 2023, **344**, 140277.
106 G. Han, C. Liu, Y. Pan, W. Macyk, S. Wageh, A. A. Al-Ghamdi and F. Xu, *Adv. Sustainable Syst.*, 2023, **7**, 2200381.
107 R. Bariki, K. Das, S. K. Pradhan, B. Prusti and B. Mishra, *ACS Appl. Energy Mater.*, 2022, **5**, 11002–11017.
108 H. Yang, H. Hou, M. Yang, Z. Zhu, H. Fu, D. Zhang, Y. Luo and W. J. Yang, *Chem. Eng. J.*, 2023, **474**, 145813.
109 J. Li, M. Li and Z. Jin, *Catal. Sci. Technol.*, 2022, **12**, 1144–1158.
110 X. Gui, Y. Zhou, Q. Liang, M. Zhou, X. Li, S. Xu and Z. Li, *Int. J. Hydrogen Energy*, 2023, **48**, 38237–38250.
111 T. Li, X. Guo, L. Zhang, T. Yan and Z. Jin, *Int. J. Hydrogen Energy*, 2021, **46**, 20560–20572.
112 K. Wang, H. Xie, Y. Li, G. Wang and Z. J. T. Jin, *J. Phys. Chem. C*, 2022, **126**, 6947–6959.
113 J. Lin, Q. Wu, J. Qiao, S. Zheng, W. Liu, L. Wu, J. Liu and Z. Zeng, *iScience*, 2023, **26**, 107132.
114 Y. Zhang, J. Xu, J. Zhou and L. Wang, *Chin. J. Catal.*, 2022, **43**, 971–1000.
115 S. Wang, B. Y. Guan, Y. Lu and X. W. D. Lou, *J. Am. Chem. Soc.*, 2017, **139**, 17305–17308.
116 Z. Cai, J. Dai, W. Li, K. B. Tan, Z. Huang, G. Zhan, J. Huang and Q. Li, *ACS Catal.*, 2020, **10**, 13275–13289.
117 M. Liu, P. Ye, M. Wang, L. Wang, C. Wu, J. Xu and Y. J. Chen, *J. Environ. Chem. Eng.*, 2022, **10**, 108436.

118 J. Liu, S. Zhu, B. Wang, R. Yang, R. Wang, X. Zhu, Y. Song, J. Yuan, H. Xu and H. Li, *Chin. Chem. Lett.*, 2023, **34**, 107749.
119 Z. Jiang, B. Cheng, L. Zhang, Z. Zhang and C. Bie, *Chin. J. Catal.*, 2023, **52**, 32–49.
120 C. Gao, J. Low, R. Long, T. Kong, J. Zhu and Y. Xiong, *Chem. Rev.*, 2020, **120**, 12175–12216.
121 J. Ran, J. Qu, H. Zhang, T. Wen, H. Wang, S. Chen, L. Song, X. Zhang, L. Jing and R. Zheng, *Adv. Energy Mater.*, 2019, **9**, 1803402.
122 A. García-Sánchez, M. Gomez-Mendoza, M. Barawi, I. J. Villar-Garcia, M. Liras, F. Gándara and V. A. de la Peña O'Shea, *J. Am. Chem. Soc.*, 2020, **142**, 318–326.
123 A. A. Zhang, R. Wang, H. B. Huang, T. F. Liu and R. Cao, *Chin. Chem. Lett.*, 2023, **34**, 107311.
124 L. Zhao, J. Bian, X. Zhang, L. Bai, L. Xu, Y. Qu, Z. Li, Y. Li and L. Jing, *Adv. Mater.*, 2022, **34**, 2205303.
125 P. Bellotti, H. M. Huang, T. Faber and F. Glorius, *Chem. Rev.*, 2023, **123**, 4237–4352.
126 M. Kim, E. You, J. Kim and S. Hong, *Angew. Chem., Int. Ed.*, 2022, **61**, e202204217.
127 Y. Sun, L. Han and P. Strasser, *Chem. Soc. Rev.*, 2020, **49**, 6605–6631.
128 M. Cai, K. Xu, Y. Li, Z. Nie, L. Zhang and S. Luo, *J. Am. Chem. Soc.*, 2021, **143**, 1078–1087.
129 X. Fan, X. Wu, F. Yang, L. Wang, K. Ludwig, L. Ma, A. Trampuz, C. Cheng and R. Haag, *Angew. Chem., Int. Ed.*, 2022, **61**, e202113833.
130 L. Li, S. Cao, Z. Wu, R. Guo, L. Xie, L. Wang, Y. Tang, Q. Li, X. Luo, L. Ma, C. Cheng and L. Qiu, *Adv. Mater.*, 2022, **34**, 2108646.
131 L. Yuan, C. Zhang, J. Wang, C. Liu and C. Yu, *Nano Res.*, 2021, **14**, 3267–3273.
132 L. Yuan, Y. Zou, L. Zhao, C. Zhang, J. Wang, C. Liu, G. Wei and C. Yu, *Appl. Catal., B*, 2022, **318**, 121859.
133 C. Xia, L. Yuan, H. Song, C. Zhang, Z. Li, Y. Zou, J. Li, T. Bao, C. Yu and C. Liu, *Small*, 2023, **19**, 2300292.
134 A. U. R. Bacha, I. Nabi, Y. Chen, Z. Li, A. Iqbal, W. Liu, M. N. Afridi, A. Arifeen, W. Jin and L. Yang, *Coord. Chem. Rev.*, 2023, **495**, 215378.
135 J. Chakraborty, I. Nath and F. Verpoort, *Chem. Soc. Rev.*, 2022, **51**, 1124–1138.
136 B. Q. L. Low, W. Jiang, J. Yang, M. Zhang, X. Wu, H. Zhu, H. Zhu, J. Z. X. Heng, K. Y. Tang, W. Y. Wu, X. Cao, X. Q. Koh, C. H. T. Chai, C. Y. Chan, Q. Zhu, M. Bosman, Y. W. Zhang, M. Zhao, Z. Li, X. J. Loh, Y. Xiong and E. Ye, *Small Methods*, 2023, 2301368.
137 M. Rashid, S. Parsaei, A. Ghoorchian, K. Dashtian and D. Mowla, *J. Ind. Eng. Chem.*, 2023, **121**, 275–286.
138 J. S. Jeyaprakash, M. Rajamani, C. L. Bianchi, M. Ashokkumar and B. Neppolian, *Ultrason. Sonochem.*, 2023, **100**, 106624.
139 Z. Li, D. Shen, X. Hu, X. Yang, Y. Li and M. Bao, *Chemosphere*, 2023, **343**, 140234.
140 H. Yang and X. Wang, *Adv. Mater.*, 2019, **31**, 1800743.
141 M. K. Albolkany, C. Liu, Y. Wang, C. H. Chen, C. Zhu, X. Chen and B. Liu, *Angew. Chem., Int. Ed.*, 2021, **60**, 14601–14608.
142 H. Y. Guan, R. J. LeBlanc, S. Y. Xie and Y. Yue, *Coord. Chem. Rev.*, 2018, **369**, 76–90.
143 M. Ahmad, S. Chen, F. Ye, X. Quan, S. Afzal, H. Yu and X. Zhao, *Appl. Catal., B*, 2019, **245**, 428–438.
144 S. Naghdi, A. Cherevan, A. Giesriegl, R. Guillet-Nicolas, S. Biswas, T. Gupta, J. Wang, T. Haunold, B. C. Bayer, G. Rupprechter, M. C. Toroker, F. Kleitz and D. Eder, *Nat. Commun.*, 2022, **13**, 282.
145 Y. Lin, C. Yang, Q. Niu and S. Luo, *Adv. Funct. Mater.*, 2022, **32**, 2108814.
146 Z. Cheng, W. Qi, C. H. Pang, T. Thomas, T. Wu, S. Liu and M. Yang, *Adv. Funct. Mater.*, 2021, **31**, 2100553.
147 C. Y. Wang, X. Zhang and H. Q. Yu, *Coord. Chem. Rev.*, 2023, **493**, 215339.
148 Y. Shi, Z. Zhao, D. Yang, J. Tan, X. Xin, Y. Liu and Z. Jiang, *Chem. Soc. Rev.*, 2023, **52**, 6938–6956.
149 S. Chen, J. J. M. Vequizo, Z. Pan, T. Hisatomi, M. Nakabayashi, L. Lin, Z. Wang, K. Kato, A. Yamakata, N. Shibata, T. Takata, T. Yamada and K. Domen, *J. Am. Chem. Soc.*, 2021, **143**, 10633–10641.
150 Y. Kageshima, Y. Gomyo, H. Matsuoka, H. Inuzuka, H. Suzuki, R. Abe, K. Teshima, K. Domen and H. Nishikiori, *ACS Catal.*, 2021, **11**, 8004–8014.
151 M. Y. Qi, M. Conte, M. Anpo, Z. R. Tang and Y. J. Xu, *Chem. Rev.*, 2021, **121**, 13051–13085.
152 Y. Liu, X. Ye, R. Li, Y. Tao, C. Zhang, Z. Lian, D. Zhang and G. Li, *Chin. Chem. Lett.*, 2022, **33**, 5162–5168.
153 A. Wang, M. Du, J. Ni, D. Liu, Y. Pan, X. Liang, D. Liu, J. Ma, J. Wang and W. Wang, *Nat. Commun.*, 2023, **14**, 6733.
154 W. Wang, G. Zhang, Q. Wang, F. Meng, H. Jia, W. Jiang and Q. Ji, *Chin. Chem. Lett.*, 2023, 109193.